



TECHNISCHE
UNIVERSITÄT
WIEN
Vienna University of Technology

DIPLOMARBEIT

Off-Axis Scintillation in Directed Atmospheric Free-Space Optical Communication Links

AUSGEFÜHRT AM
Institut für Angewandte Physik
Technische Universität Wien

IN ZUSAMMENARBEIT MIT DEM
Institut für Kommunikation und Navigation
Deutsches Zentrum für Luft- und Raumfahrt

unter der Anleitung von
Ao.Univ.Prof. DI Dr.techn. Martin Gröschl
Dr.-Ing. Dirk Giggenbach
Dr. Ramon Mata Calvo

EINGEREICHT AN
der Technischen Universität Wien
Fakultät für Physik

VON

Florian Peter Pribahsnik

Malfattigasse 1-5/8/18
1120 Wien

February 19, 2016

Unterschrift StudentIn

*In the memory of my beloved father,
who provided me with all his support,
but who could not see this work finalized anymore.*

Our time together was way too short.

Acknowledgment

I would like to thank my Professor Martin Gröschl for the possibility to start this thesis under his supervision. He supplied me with the most valuable advice imaginable and supported me also in complicated times. He was always very appreciative and solution-oriented. I further thank my colleagues at DLR for the productive discussions and our fun time together. Lastly, I want to thank my supervisors Dirk Giggenbach and Ramon Mata Calvo at the German Aerospace Center for giving me the opportunity of writing my thesis abroad in this interesting field of work.

Abstract

The topic of this thesis is located in the field of free-space optics. Free-space optics is a possible solution for the rising demand for bandwidth in communication. Free-space optics modulates data on an infrared laser beam in order to connect satellites or aircraft with ground stations or to establish a link between buildings.

The challenges to be met within this technology are disturbances that evolve when the beam propagates through the turbulent media atmosphere. While spreading through the air, the beam interferes with itself and gets bended because of different sized eddies. The scintillation index is a parameter that describes the fluctuation of intensity at a point.

Although existing theory predicts a quadratic increase of the scintillation index if moved off-axis, the prediction is just valid up to a distance equal to the beam radius. Further interpolation leads to nonphysical results and for this reason, the off-axis scintillation index was measured.

The tasks of this thesis included the design of a setup using an already existing test track. The distance of this track was 735m and measurements were taken on different days in order to cover different values of the turbulence index. The measurements taken were post-processed to reduce any unwanted influences. Furthermore, the measurements were evaluated in untracked and tracked mode in order to analyze the effects of tracking on the scintillation index profile.

Independent of the turbulence index and other parameters it was measured that the scintillation index reaches a maximum and then decreases until it reaches a saturation level in the order of magnitude of the on-axis scintillation index. According to these measurements, the maximum itself is located between the single and double beam radius off-axis and reaches a maximum value approximately three times as large as the on-axis value.

Zusammenfassung

Die hier vorliegende Masterarbeit wurde im Themenkomplex der Freistrahlkommunikation geschrieben. Freistrahlkommunikation ist ein möglicher Lösungsweg, um dem wachsenden Bedarf an Bandbreite in der Kommunikationstechnologie zu begegnen, indem man mit Hilfe eines modulierten Infrarot-Laserstrahls Daten überträgt. Diese Technik kann verwendet werden, um Satelliten mit der Erde oder Flugzeuge mit Bodenstationen zu verbinden, beziehungsweise um Datenverbindungen zwischen Gebäuden zu errichten.

Die Schwierigkeit bei dieser Art der Übertragung von Daten ist die Störung des Signals aufgrund der turbulenten Atmosphäre. Bei der Ausbreitung des Strahls in der Atmosphäre kommt es durch die verschiedenen großen Verwirbelungen der Luft zu Interferenzen des Strahls mit sich selbst sowie zur Brechung des gesamten Strahls. Eine Kenngröße dieser Störeffekte ist der Szintillationsindex, der die Varianz der Helligkeit an einem Punkt beschreibt.

Die aktuelle Theorie zum Szintillationsindex abseits der optischen Achse (off-axis) besagt, dass der Szintillationsindex quadratisch mit der Entfernung von der optischen Achse zunimmt. Diese Vorhersage ist aber nur innerhalb des einfachen Strahlradius gültig. Da eine weitere Interpolation dieser Theorie physikalisch nicht sinnvoll ist, wurde der Szintillationindexverlauf in Abhängigkeit des Abstands zur optischen Achse vermessen.

Die Aufgabe bestand darin, ein Setup zu entwerfen, das die Vermessung über eine bestehende Teststrecke ermöglicht. Die Teststrecke weist eine Länge von 735 m auf. Es wurden für die Messung zwei verschiedene Strahldivergenzen verwendet und die Messungen wurden an verschiedenen Tagen durchgeführt, um verschiedene Turbulenzindizes zu erhalten. Die Messungen wurden elektronisch ausgewertet und so weit als möglich von allen störenden Einflüssen befreit. Auch wurden alle Messungen sowohl *tracked* als auch *untracked* ausgewertet und analysiert, um den Effekt des Tracking auf den Szintillationsindexverlauf zu verstehen.

Unabhängig von der Turbulenzstärke und anderen Parametern wurde nachgewiesen, dass der Szintillationsindex ein Maximum erreicht und dann wieder abfällt, woraufhin sich ein Sättigungswert in der Größenordnung des Szintillationsindex auf der optischen Achse einstellt. Das Maximum liegt den Messungen zufolge zwischen dem einfachen und dem doppelten Strahlradius und erreicht ungefähr den dreifachen Wert des Wertes auf der optischen Achse.

Contents

1	Motivation	1
1.1	State of the Art	1
1.2	Outlook	1
2	Theory	3
2.1	Preamble	3
2.2	Random Process	3
2.2.1	Mean Value and Variance	3
2.2.2	Stationary Process	4
2.2.3	Ergodic Process	4
2.2.4	Auto-Correlation and Auto-Covariance Functions	4
2.2.5	Power Spectral Density Function	4
2.3	Turbulent Air	4
2.3.1	Velocity Fluctuations	5
2.3.2	Temperature Fluctuations	6
2.3.3	Optical Fluctuations	6
2.3.4	Kolmogorov spectrum	7
2.4	Gaussian Beam	7
2.4.1	Derivation	7
2.4.2	Plane Wave	8
2.4.3	Spherical Wave	8
2.4.4	Gaussian Wave	8
2.4.5	Solving Helmholtz Equation	9
2.4.6	Input Plane Beam Parameter	9
2.4.7	Output Plane Beam Parameters	10
2.5	Existing Models	11
2.5.1	Weak Fluctuations	11
2.5.2	Strong Fluctuations	14
2.5.3	Scintillation Simulation beyond W	15
3	Measuring Principles	17
3.1	Cassegrain Telescope	17
3.2	Collimator	18
3.3	Shearing Interferometer	18
3.4	InGaAs Camera	19
3.5	Laser	19
3.6	Requirements	20

3.7	Design	20
3.8	Realization	23
3.8.1	Large Divergence	23
3.8.2	Small Divergence	25
4	Preliminary Setup	27
4.1	Tilt Rotation Platform	27
4.2	Testlink and Alignment	28
4.3	Measurement	28
4.4	Problems	28
4.4.1	Rubber Floor Plate	29
4.4.2	Small Magnification	30
4.4.3	Interference Pattern	31
4.4.4	Donut Shape	31
4.4.5	Faster Measurements	34
4.5	Results	34
5	Optimal Setup	36
5.1	Improvements	36
5.1.1	Greater Magnification	36
5.1.2	New Collimator	37
5.1.3	Alignment Scope	38
5.1.4	Installation Site and Source	38
5.2	Measurement	38
5.3	Post Processing	41
6	Results and Analysis	46
6.1	20.07.2015	46
6.2	21.07.2015	49
6.3	22.07.2015	52
6.4	Conclusion and Outlook	55
7	Appendix	56
	References	56
	Acronyms	58
	List of Symbols	58
	List of Figures	59
	List of Tables	62
	Fitting Values	63

Chapter 1

Motivation

1.1 State of the Art

Free-space optical communication (FSO) is a technology that uses light propagating through free space to transfer information. It can be understood similar to classic wireless technology, but in another spectral range. There are different scenarios where this technology can be used:

- Point-to-point connections between two points on the surface of the earth. Due to attenuation connected to weather effects, the distance over which a stable connection can be established is relatively limited.
- Satellite-to-satellite connections in outer space. As there are no atmospheric limitation effects on the beam, diffraction is the only limiting factor.
- Earth-to-satellite uplinks and downlinks. These two scenarios have the possibility to significantly increase data rates between satellites and the earth and to provide remote areas with internet.
- Earth-to-aircraft. This gives the possibility of high data rate downlinks from planes to ground stations for emergency purposes.

As can be seen in the applications mentioned above, this technology can be used in a wide range. NASA recently demonstrated with the Optical Payload for Lasercomm Science (OPALS) that the technology works quite well as a satellite downlink. The German Aerospace Center (DLR) also made some advances in FSO by establishing an optical link between a ground station (TOGS) and aircraft equipped with a terminal.

1.2 Outlook

Due to the significantly higher data rates in combination with very narrow beam divergence provided by FSO when compared to conventional radio frequency links, link budgets can be improved. Another advantage is the low energy consumption of the transmitter as well as the relatively tap-proof data stream which are connected to the very small angle of radiation and the missing side lobes. Furthermore, interference between two systems does not pose a challenge and so far, there are no regulations by authorities regarding this technology.

This advantages make this technology very interesting for military or space applications.

Challenges that need to be faced besides the necessity for very accurate pointing and tracking mostly arise from the propagation through atmosphere. The atmosphere is not a homogeneous substance. Due to temperature fluctuations, wind and other effects, the atmosphere is split up in eddies of various sizes and optical properties. These eddies can cause beam refraction and self-interference, leading to several optical effects. One of the effects is the scintillation characterized by the scintillation index. This scintillation index can be split into a part on the optical axis and one off-axis. Due to other effects caused by the propagation through atmosphere and the trend of mounting these terminals on various type of aircraft, the index is highly unlikely to be exactly on axis and so the understanding and estimation of the off-axis scintillation index behavior is crucial for the application of this technology.

Chapter 2

Theory

2.1 Preamble

When starting to work in Free Space Optics (FSO), basic physical problems need to be faced. A source that is widely used and recommended is, *Laser beam propagation through random media*, a book not only discussing the principles of laser beam propagation through random media, as the title says, but further representing and summarizing the latest efforts in this field. The book was written by Larry C. Andrews and Ronald L. Phillips in 2005. It is structured in a way to pick up the intrigued reader at the fundamental basics and from there on guiding him or her to the latest results acquired. This book covers hundreds of papers and other sources listed at the end of each chapter. Therefore, the theoretical section of this thesis relies entirely on this book, if not characterized otherwise.

2.2 Random Process

A random or stochastic process is a mathematical description of random events over time. Such a statistical process consists of many realizations $x(t)$. If a random process $x(t)$ is measured multiple times t_1, t_2, \dots, t_n , a distribution of measured value $x(t_1), x(t_2), \dots, x(t_n)$ will be found. The probability to measure a certain value is given by the joint probability density function (PDF) for a random process $x(t)$,

$$p_x(x_1, t_1), \quad (2.1)$$

or, for n variables,

$$p_x(x_1, t_1; x_2, t_2; \dots; x_n, t_n). \quad (2.2)$$

2.2.1 Mean Value and Variance

Brackets $\langle \rangle$ are used to express the ensemble average. The expected value of a random process $x(t)$ is defined as

$$\langle x(t) \rangle = \int_{-\infty}^{\infty} x p_x(x, t) dx = m(t). \quad (2.3)$$

The variance is defined as

$$\sigma_x^2(t) = \langle x^2(t) \rangle - \langle x(t) \rangle^2 = \int_{-\infty}^{\infty} (x(t) - m(t))^2 p_x(x, t) dx. \quad (2.4)$$

2.2.2 Stationary Process

If the first order PDF of a random process is time independent, $p_x(x, t) = p_x(x)$, the second form depends only on the time difference $p_x(x_1, t_1; x_2, t_2) = p_x(x_1, x_2; t_1 - t_2)$ and all margins further depend only on the difference between $\tau = t_1 - t_2$. If this is the case, the process is called “stationary”. In other words, the PDF of a stationary process does not change over time.

2.2.3 Ergodic Process

The PDF of a random process is defined by the ensemble average. However, this quantity can normally not be observed, as one experiment only has one possible realization. Usually, the average over time of a random process is measured. If the ensemble average and the average over time are the same, the process is called “ergodic”. Any ergodic process must also be stationary.

2.2.4 Auto-Correlation and Auto-Covariance Functions

The auto-correlation function between values of a random stationary process is defined as

$$R_x(t_1, t_2) = R_x(\tau) = \langle x(t_1)x(t_2) \rangle = \int \int_{-\infty}^{\infty} x_1 x_2 p_x(x_1, x_2; \tau) dx_1 dx_2. \quad (2.5)$$

The auto-covariance function of a random process is defined as

$$B_x(t_1, t_2) = \langle (x(t_1) - \langle x(t_1) \rangle) \cdot (x(t_2) - \langle x(t_2) \rangle) \rangle. \quad (2.6)$$

If this process is stationary, it can be written as

$$B_x(\tau) = R_x(\tau) - m^2. \quad (2.7)$$

Although normally, all margins and PDFs are required to be independent of the time origin, it is possible to define a less strict definition of a stationary process. In a wider sense, a process is stationary if $\langle x(t) \rangle = \text{const.}$ and $B_x(\tau)$ depends only on the time difference $\tau = t_1 - t_2$ (see: Andrew Philips, p.39).

2.2.5 Power Spectral Density Function

According to the Wiener-Khinchin theorem, the power spectral density function (PSD) $S_x(\omega)$ of a stationary process in a wide sense is the Fourier transformation of its covariance function $B_x(\tau)$:

$$S_x(\omega) = \frac{1}{2\pi} \int_{-\infty}^{\infty} e^{-i\omega\tau} B_x(\tau) d\tau \quad (2.8)$$

and

$$B_x(\tau) = \int_{-\infty}^{\infty} e^{i\omega\tau} S_x(\omega) d\omega. \quad (2.9)$$

2.3 Turbulent Air

Considering air as a flowing viscous fluid, there are two possible ways of motion: laminar flow and turbulent flow. Commonly, these two distinct states are distinguished by the Renold’s number. Renold’s number was initially introduced to study scaled fluid motion problems. A scaled version

of a problem has to have the same Renold's number in order to behave the same. The Renold's number is defined as:

$$Re = \frac{\text{inertial force}}{\text{viscous force}} = \frac{vl}{\eta}. \quad (2.10)$$

Further, the critical Renold's number is used to describe the point beyond which the fluid is considered as turbulent. Close to the ground, the Renold's number can be calculated by:

$$\left. \begin{array}{l} v \sim 1 \text{ m/s to } 5 \text{ m/s} \\ l \sim 2 \text{ m} \\ \eta \sim 0.15 \times 10^5 \text{ m}^2/\text{s} \end{array} \right\} RE \sim 10^5. \quad (2.11)$$

Such a high value characterizes very turbulent motions. The mixing in turbulence causes eddies in different sizes.

2.3.1 Velocity Fluctuations

Energy from shear winds and convection of air leads to eddies of various sizes. As illustrated in fig. 2.1, Lewis Fry Richardson proposed to divide the spectra of turbulence into three categories. In the first region, energy is injected. In the third area, the kinetic energy is converted into

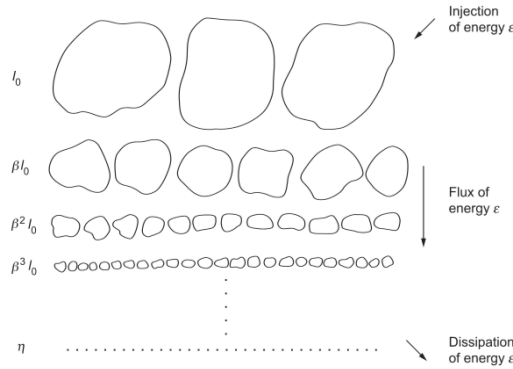


Figure 2.1: Three regions of turbulence. Source: [1].

internal energy. To effectively transform the energy in the dissipation sub-range, big eddies break up into smaller ones in the middle area called “inertial sub-range”. The sizes of the eddies in this range are between the outer and the inner scale of turbulence, L_0 and l_0 , respectively. The lower limit of the eddy size-range is given by the Kolmogorov micro scale,

$$l_0 \sim \eta = \left(\frac{\nu^3}{\epsilon}\right)^{\frac{1}{4}}, \quad (2.12)$$

setting the minimum eddy size around 1×10^{-3} m to 10×10^{-3} m. The outer scale is proportional to $\epsilon^{\frac{1}{2}}$ and is typically around 100 m. Kolmogorov showed that the structure function of the longitudinal velocity satisfies the 2/3 power law and can be written as

$$D_R(R) = \langle (v_1 - v_2)^2 \rangle = C_v^2 R^{\frac{2}{3}}, \quad l_0 \ll R \ll L_0, \quad (2.13)$$

where r is the eddy size and C_v is the velocity structure constant defined by the average energy dissipation ϵ :

$$C_v^2 = 2\epsilon^{\frac{2}{3}}. \quad (2.14)$$

It can be assumed that in the dissipation range, the structure is isotropic and statistically homogeneous. The previously introduced structure function corresponds to the following three-dimensional power spectrum

$$\Phi_R(k) = 0.066\epsilon^{\frac{2}{3}}\kappa^{-\frac{11}{3}} = 0.033C_v^2\kappa^{-\frac{11}{3}}, \quad \frac{1}{L_0} \ll \kappa \ll \frac{1}{l_0}. \quad (2.15)$$

2.3.2 Temperature Fluctuations

Kolmogorov's idea was later extended to the theory of temperature fluctuations. To do so, it is assumed that the temperature is a passive scalar with means that it does not exchange energy with the velocity turbulence. With this assumption, the following structure function is

$$D_T(R) = \langle (T_1 - T_2)^2 \rangle = C_T^2 R^{\frac{2}{3}}, \quad l_0 \ll R \ll L_0, \quad (2.16)$$

where C_T is the temperature structure constant. This structure function relates to a the three-dimensional power spectrum

$$\Phi_T(k) = -\frac{1}{4\pi}\beta\chi\epsilon^{-\frac{1}{3}}\kappa^{-\frac{11}{3}} = 0.033C_T^2\kappa^{-\frac{11}{3}}, \quad \frac{1}{L_0} \ll \kappa \ll \frac{1}{l_0}, \quad (2.17)$$

where β is the Obukhov-Corrsin constant and χ the rate of dissipation of the mean-squared fluctuation.

2.3.3 Optical Fluctuations

“Refractive-index fluctuations” or so called “optical fluctuations” arise through the combination of eddies from velocity fluctuations and temperature fluctuations. In general, the dependence of time in optical fluctuations is suppressed so that the wavelength of the wave does not change. In this case, the fluctuation can be written as

$$n(\vec{R}) = n_0 + n_1(\vec{R}) \cong 1 + n_1(\vec{R}). \quad (2.18)$$

For wavelengths in the optical or infrared (IR) spectrum, $n(\vec{R})$ can be written as

$$n(\vec{R}) = 1 + 77.6 \times 10^{-6}(1 + 7.52 \times 10^{-15}\lambda^{-2})\frac{p(\vec{R})}{T(\vec{R})} \cong 1 + 79 \times 10^{-6}\frac{p(\vec{R})}{T(\vec{R})}. \quad (2.19)$$

Under the assumption that the optical fluctuation is isotropically and statistically homogeneous, the structure function can be written as

$$D_n(r) = C_n^2 R^{-\frac{2}{3}} \quad l_0 \ll R \ll L_0, \quad (2.20)$$

where index of refraction structure constant (C_n^2) and l_0 is defined as

$$l_0 = 7.4\eta = 7.4\left(\frac{\nu^3}{\epsilon}\right)^{\frac{1}{4}}. \quad (2.21)$$

Using eq. (2.19), C_n^2 can be written as

$$C_n^2 = (79 \times 10^{-6}\frac{p}{T^2})^2 C_T^2 \quad (2.22)$$

C_n^2 can be measured averaged over a distance using a scintillometer. Typical values of C_n^2 are around $10^{-17} \text{ m}^{-\frac{2}{3}}$ to $10^{-13} \text{ m}^{-\frac{2}{3}}$, with the latter corresponding to strong turbulence. Regarding the assumption concerning isotropy and statistical homogeneity, the power spectrum of the optical fluctuation can be written as

$$\Phi_n(k) = \frac{1}{(2\pi)^3} \iiint_{-\infty}^{\infty} B_n(R) e^{-i\vec{k}\vec{R}} d^3r = \frac{1}{2\pi^2 k} \int_0^{\infty} B_n(R) \sin(kR) R dr. \quad (2.23)$$

Performing the inverse Fourier transformation, it can be concluded that

$$B_n(k) = \frac{4\pi}{R} \int_0^{\infty} k \Phi_n(k) \sin(kR) dr \quad (2.24)$$

and the structure function can be written as

$$D_n(R) = 8\pi \int_0^{\infty} k^2 \Phi_n(k) \left(1 - \frac{\sin(kR)}{kR}\right) dk. \quad (2.25)$$

2.3.4 Kolmogorov spectrum

In the Kolmogorov spectrum, it is assumed that the fluctuations of pressure and humidity are small enough to be neglected and that the refractive-index fluctuations are governed mainly by the temperature fluctuations:

$$\Phi_n(\kappa) = 0.33 C_n^2 \kappa^{-\frac{11}{3}}, \quad \frac{1}{L_0} \ll \kappa \ll \frac{1}{l_0}. \quad (2.26)$$

There further exist some more advanced spectra that avoid the problems arising from inner and outer scale. These are called Tatarskii, von Kármán, exponential and modified atmospheric spectrum. These spectra go beyond the scope of this thesis, but are further discussed in detail in the book by Andrew and Philips [2].

2.4 Gaussian Beam

2.4.1 Derivation

The wave equation is a differential equation in order to describe waves:

$$\nabla^2 u = \frac{1}{c^2} \frac{\partial^2 u}{\partial t^2}. \quad (2.27)$$

The time independent solutions to this equation can be further simplified to the so-called ‘‘Helmholtz’ equation’’:

$$\nabla^2 U_0 + k^2 U_0 = 0. \quad (2.28)$$

Here, k is the wave number defined as $k = \frac{2\pi}{\lambda}$. Finally, a paraxial approximation can be made for Helmholtz’ equation. First, the assumption has to be made that the wave propagates along the z -axis and that the surrounding optical field is rotationally symmetric at all times. The equation can then be transformed in cylindrical coordinates:

$$\frac{1}{r} \frac{\partial}{\partial r} \left(r \frac{\partial V}{\partial r} \right) + \frac{\partial^2 V}{\partial z^2} + 2ik \frac{\partial V}{\partial z} = 0. \quad (2.29)$$

It is further assumed that the spreading distance perpendicular to the z -axis is very small compared to the propagation distance in z -direction. Under this assumptions, it can be concluded that

$$\begin{aligned}\sin \varphi &\approx \varphi \\ \tan \varphi &\approx \varphi.\end{aligned}\tag{2.30}$$

This is done in order to neglect the term

$$\left| \frac{\partial^2 V}{\partial z^2} \right| \ll |k^2 A|,\tag{2.31}$$

and results in Helmholtz' equation including the paraxial approximation:

$$\frac{1}{r} \frac{\partial}{\partial r} \left(r \frac{\partial V}{\partial r} \right) + 2ik \frac{\partial V}{\partial z} = 0.\tag{2.32}$$

The solution to this equation will be discussed later on.

2.4.2 Plane Wave

A plane wave is a wave with constant frequency and amplitude and a plane infinite wavefront propagating in space. The mathematical description of such a wave is given by:

$$U_0(r, z) = A_0 e^{i\varphi_0 + ikz}.\tag{2.33}$$

Due to the fact that the source of a plane wave is an assumed infinite plane, a true plane wave can not be observed in reality.

2.4.3 Spherical Wave

A spherical wave is a wave constant in frequency with a spherical wavefront propagating in space. The source of such a wave is a point from where energy dissipates in every direction. Therefore, the amplitude of such waves is decreasing by $1/r$ and its mathematical description is given by

$$U_0(r, z) = \frac{A_0}{4\pi z} e^{ikz + \frac{ikr^2}{2z}} \quad z > 0.\tag{2.34}$$

2.4.4 Gaussian Wave

A Gaussian beam of the lowest order, also called TEM_{00} , is a wave with a Gaussian distribution in the plane perpendicular to the propagating direction. The radius of curvature F_0 defines the behavior of the Gaussian beam when propagating. Its value is determined by the position of the transmitter in the general beam profile. I.e., F_0 determines if the beam is divergent ($F_0 < 0$), focused ($F_0 > 0$) or collimated ($F_0 = 0$). W is called the "beam radius". It is defined as the radius where the field amplitude has decreased to $\frac{1}{e}$. W_0 denotes the minimal beam radius at the beam waist. If the beam waist is located at $z = 0$, the corresponding amplitude at this location is a_0 and the wave can be written as:

$$U_0(r, z) = a_0 e^{-\frac{r^2}{W_0^2} - \frac{ikr^2}{2F_0}},\tag{2.35}$$

whereas r is the distance from the optical axis, z , defined as $r^2 = \sqrt{x^2 + y^2}$. For subsequent definitions of beam parameters, it is convenient to introduce a beam parameter α_0 :

$$\alpha_0 = \frac{2}{kW_0^2} + i\frac{1}{F_0},\tag{2.36}$$

$$U_0(r, z) = a_0 e^{-\frac{1}{2}\alpha_0 k r^2}. \quad (2.37)$$

The amplitude A_0 and the phase φ_0 can be written as:

$$\begin{aligned} A_0 &= a_0 e^{-\frac{r^2}{W_0^2}}, \\ \varphi_0 &= -\frac{k r^2}{2F_0}. \end{aligned} \quad (2.38)$$

It always has to be kept in mind that, if the beam has a smaller divergence, the beam waist gets broader and vice versa. This is due to the requirement that the product of divergence and beam waist remains constant.

$$\theta \cdot W_0 \approx \frac{\lambda}{\pi} \quad (2.39)$$

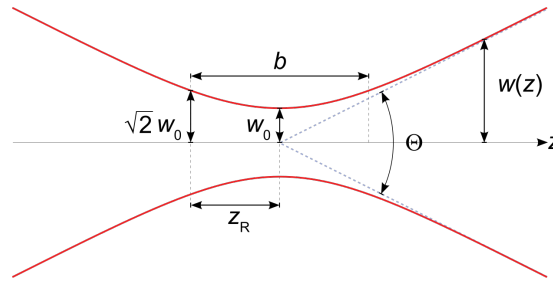


Figure 2.2: Gaussian Beam principle. Source: [3].

2.4.5 Solving Helmholtz Equation

In order to solve Helmholtz' equation, solutions with a Gaussian function are assumed. Starting with

$$U(r, z) = A(z) e^{-\frac{1}{p(z)} \left(\frac{\alpha_0 k r^2}{2} \right)} \quad (2.40)$$

and inserting this into equation 2.27, it follows that

$$\alpha_0 k^2 r^2 A(z) + i \alpha_0 k^2 r^2 A(z) p'(z) - 2 \alpha_0 k A p(z) + 2 i k A'(z) p^2(z) \quad (2.41)$$

By separating the terms by powers of r and setting each of them to 0, two equations result which, when solved give the following solution of the Helmholtz equation:

$$U_0(r, z) = -\frac{1}{1 + i \alpha_0 z} e^{i k z + \frac{i k}{2z} \left(\frac{i \alpha_0 z}{1 + i \alpha_0 z} \right)} \quad (2.42)$$

2.4.6 Input Plane Beam Parameter

In this section, the Gaussian solution of the Helmholtz equation is rewritten to quantities of the transmitter (i.e., input) plane. By defining two new variables,

$$\begin{aligned} \Theta_0 &= 1 - \frac{1}{F_0}, \\ \Lambda_0 &= \frac{2z}{k W_0^2}, \end{aligned} \quad (2.43)$$

the solution 2.42 can be rewritten as

$$U_0(r, z) = \frac{1}{\sqrt{\Theta_0^2 + \Lambda_0^2}} e^{-\frac{r^2}{w^2}} e^{i(kz - \varphi - \frac{kr^2}{2F})}, \quad (2.44)$$

with

$$\begin{aligned} \varphi &= \arctan \frac{\Lambda_0}{\Theta_0}, \\ W &= W_0 \sqrt{\Theta_0^2 + \Lambda_0^2}, \\ F &= \frac{F_0(\Theta_0^2 + \Lambda_0^2)(\Theta_0 - 1)}{\Theta_0^2 + \Lambda_0^2 - \Theta_0}. \end{aligned} \quad (2.45)$$

φ is called the ‘‘longitudinal phase shift’’, W is the spot size radius and F is the radius of curvature. With this form of the U_0 , the amplitude after a propagating distance can be identified as

$$A = \frac{1}{\sqrt{\Theta_0^2 + \Lambda_0^2}}. \quad (2.46)$$

2.4.7 Output Plane Beam Parameters

As in the previous section, the solution of the Helmholtz equation can be written in parameters according to the receiver (i.e., output) plane. This is done by defining three new variables:

$$\begin{aligned} \Theta &= \frac{\Theta_0}{\Theta_0^2 + \Lambda_0^2}, \\ \Lambda &= \frac{\Lambda_0}{\Theta_0^2 + \Lambda_0^2}, \\ \bar{\Lambda} &= 1 - \Lambda, \\ \bar{\Theta} &= 1 - \Theta. \end{aligned} \quad (2.47)$$

With these variables, the solution 2.42 can be rewritten as

$$U_0(r, z) = \sqrt{\Theta^2 + \Lambda^2} e^{-\frac{k\Lambda r^2}{2z}} e^{i(kz - \varphi - \frac{k\bar{\Lambda}r^2}{2z})}, \quad (2.48)$$

with

$$\begin{aligned} \varphi &= \arctan \frac{\Lambda}{\Theta}, \\ W &= \frac{W_0}{\sqrt{\Theta^2 + \Lambda^2}}, \\ F &= \frac{F_0(\Theta^2 + \Lambda^2 - \Theta)}{(\Theta^2 + \Lambda^2)(\Theta - 1)}. \end{aligned} \quad (2.49)$$

Here, σ_R is the Rytov variance defined as

$$\sigma_R^2 = 1.23 C_n^2 k^{\frac{7}{6}} l^{\frac{11}{6}}. \quad (2.50)$$

Here, C_n^2 is the refractive index structure parameter.

2.5 Existing Models

In theory, there is a distinction between two scenarios with respect to the strength of the turbulence in the atmosphere and the resulting scintillation index. If the scintillation index of a beam is lower than one, this atmospheric distortions is considered as a “weak turbulence”. Otherwise, its is referred to as a “moderate to strong” or “strong turbulence”. As shown in Andrew and Phillips, these conditions can be transformed into two conditions which can be validated before doing any serious calculations:

$$\begin{aligned}\sigma_R^2 &< 1, \\ \sigma_R^2 \Lambda^{\frac{5}{6}} &< 1.\end{aligned}\tag{2.51}$$

If any of the conditions in 2.51 are violated, the situation has to be considered as moderate to strong or strong.

Rytov Approximation

To solve the Helmholtz equation

$$\nabla^2 U + k^2 n^2(R)U = 0,\tag{2.52}$$

the Rytov approximation first writes the electromagnetic field as

$$U(r, L) = U_0(r, L)e^{\Phi(r, L)}, \Phi(r, L) = \Phi_1(r, L) + \Phi_2(r, L) \cdots ,\tag{2.53}$$

where Φ holds the turbulence.

Statistical Moments

Statistical moments are descriptive parameters in stochastic. With the description of the electromagnetic Field U_0 , they can be written as

$$\langle U_0(r, L)e^{\Phi(r, L)} \rangle = \langle U_0(r, L)e^{\Phi_1(r, L) + \Phi_2(r, L)} \rangle,\tag{2.54}$$

$$\begin{aligned}\langle U_0(r, L)e^{\Phi(r_1, L)} \cdot U_0^*(r, L)e^{\Phi^*(r_2, L)} \rangle = \\ \langle U_0(r, L)e^{\Phi_1(r_1, L) + \Phi_2(r_1, L)} \cdot U_0^*(r, L)e^{\Phi_1^*(r_2, L) + \Phi_2^*(r_2, L)} \rangle\end{aligned}\tag{2.55}$$

and

$$\begin{aligned}\langle U_0(r, L)e^{\Phi(r_1, L)} \cdot U_0^*(r, L)e^{\Phi^*(r_2, L)} \cdot U_0^*(r, L)e^{\Phi^*(r_3, L)} \cdot U_0^*(r, L)e^{\Phi^*(r_4, L)} \rangle = \\ \langle U_0(r, L)e^{\Phi_1(r_1, L) + \Phi_2(r_1, L)} \cdot U_0^*(r, L)e^{\Phi_1^*(r_2, L) + \Phi_2^*(r_2, L)} \cdot \\ U_0^*(r, L)e^{\Phi_1^*(r_3, L) + \Phi_2^*(r_3, L)} \cdot U_0^*(r, L)e^{\Phi_1^*(r_4, L) + \Phi_2^*(r_4, L)} \rangle.\end{aligned}\tag{2.56}$$

2.5.1 Weak Fluctuations

If none of these conditions in ref.2.51 are violated, the situation is described by the theory of weak fluctuation. This theory uses the Rytov approximation to solve the Helmholtz equation.

Beam Wander

As discussed before, a Gaussian beam spreads after the beam waist. Additionally to this effect of Gaussian optics, the beam is spread because of the turbulence eddies. It can be shown that this effect arises mostly from turbulence cells in the size of the beam or bigger. These eddies cause a small deflection from the optical axis of the beam. Hence the effect on the receiver is greater if the deflection happens closer to the transmitter. Such small refraction can be seen as “dancing” or wandering of the instantaneous beam center on the receiver plane as seen in fig. 2.3. The long

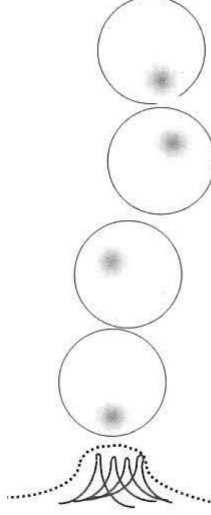


Figure 2.3: Wandering of the instantaneous beam center. Source: [2].

term spot is broadened and distorted. The size of the long term spot W_{LT} can be deduced from the second moment on the same place ($r_1 = r_1$) and is given by

$$W_{LT}^2 = W^2(1 + T) = W^2(1 + 1.33\sigma_R^2\Lambda^{\frac{5}{6}}). \quad (2.57)$$

The distortion can be characterized by the pointing error variance σ_{pe}^2 , which is

$$\sigma_{pe}^2 \approx 7.25C_n^2L^3W_0^{-\frac{1}{3}} \int_0^1 \xi^2 \left(\frac{1}{|\Theta_0 + \bar{\Theta}_0\xi|^{\frac{1}{3}}} - \left(\frac{\kappa_r^2W_0^2}{1 + \kappa_r^2W_0^2(\Theta_0 + \bar{\Theta}_0)^2} \right)^{\frac{1}{6}} \right) d\xi \quad (2.58)$$

for every wavefront curvature radius. κ_r is defined as

$$\kappa_r = \frac{C_r}{r_0} \quad C_r \sim 2\pi \quad (2.59)$$

and r_0 is the atmospheric coherence. The wandering of the beam can be split into two different movements depending on the respective timescales:

$$W_{LT}^2 = \langle r_c^2 \rangle^{\frac{1}{2}} + W_{ST}^2. \quad (2.60)$$

According to Andrew and Phillips, $\langle r_c^2 \rangle$ can be written as

$$\langle r_c^2 \rangle = 7.25C_n^2L^3W_0^{-\frac{1}{3}} \int_0^1 \xi^2 \left(\frac{1}{|\Theta_0 + \bar{\Theta}_0\xi|^{\frac{1}{3}}} - \left(\frac{\kappa_0^2W_0^2}{1 + \kappa_0^2W_0^2(\Theta_0 + \bar{\Theta}_0)^2} \right)^{\frac{1}{6}} \right) d\xi \quad (2.61)$$

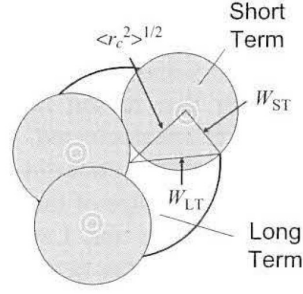


Figure 2.4: Separation of the two beam wander effects. Source: [2]

for every wavefront curvature radius. κ_0 is the outer scale parameter defined as

$$\kappa_0 = \frac{C_0}{L_0} \quad C_0 \text{ typically : } 1 \leq C_0 \leq 8\pi. \quad (2.62)$$

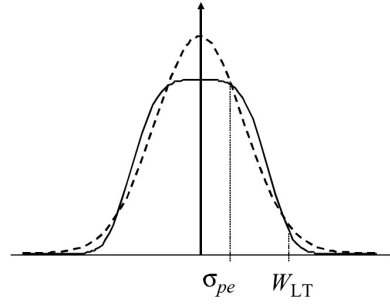


Figure 2.5: Broadened beam after propagating through turbulent media. Source: [2]

Scintillations

Scintillations are intensity fluctuation. These fluctuations are characterized by the scintillation index, which is an irradiation variance variance scaled by the squared mean irradiation:

$$\sigma_I^2(r, L) = \frac{\langle I^2(r, L) \rangle}{\langle I(r, L) \rangle^2} - 1. \quad (2.63)$$

To simplify studies on these phenomena, the scintillation index is split into two parts. One part is the scintillation index along the optical axis and the other is an off-axis component which contributes only if the beam is not positioned on the optical axis:

$$\sigma_I^2(r, L) = \sigma_{I,r}^2(r, L) + \sigma_{I,l}^2(L). \quad (2.64)$$

As Andrew and Phillips have shown, the radial term of the scintillation index, of an untracked beam, can be approximated by

$$\sigma_{I,r}^2(r, L) \approx 4.42\sigma_R^2\Lambda^{\frac{5}{6}}\frac{r^2}{W^2} \quad r < W \quad (2.65)$$

and the longitudinal part by

$$\sigma_{I,l}^2(L) \approx 3.86\sigma_R^2(0.4((1+2\Theta)^2 + 4\Lambda^2)^{\frac{5}{12}} \cdot \cos(\frac{5}{6}\arctan(\frac{1+2\Theta}{2\Lambda})) - \frac{11}{16}\Lambda^{\frac{5}{6}}). \quad (2.66)$$

2.5.2 Strong Fluctuations

If one of the inequalities in eq. (2.51) is violated, the turbulence is considered as strong. Other than in the case of weak fluctuation, the parabolic equation method is used to get the statistical moments.

Long-Term Spot Size

The long-term spot size of a Gaussian beam under strong fluctuation is given as

$$W_{LT} = W\sqrt{1 + \frac{4q\Lambda}{3}}. \quad (2.67)$$

The turbulence parameter q is derived depending on ρ_{pl} :

$$q \begin{cases} 1.22(\sigma_r^2)^{\frac{5}{6}}, & \rho_{pl} \gg l_0 \\ 1.33\sigma_r^2(\frac{L}{kl_0^2})^{\frac{1}{6}}, & \rho_{pl} \ll l_0 \end{cases} \quad (2.68)$$

whereas ρ_{pl} is the spatial coherence radius of a spherical beam wave and ρ_0 is the spatial coherence radius of a Gaussian beam wave connected as follows:

$$\frac{\rho_0}{\rho_{pl}} = \sqrt{\frac{3 + 4q\Lambda}{1 + \Theta + \Theta^2 + \Lambda^2 + q\Lambda}}, \quad q \gg \Lambda. \quad (2.69)$$

Beam Wander

As in the case of weak fluctuation, the beam wander effects are split up in two parts depending on the timescale:

$$W_{LT}^2 = \langle r_c^2 \rangle^{\frac{1}{2}} + W_{ST}^2, \quad (2.70)$$

where the slow term $\langle r_c^2 \rangle$ is calculated as

$$\langle r_c^2 \rangle = 7.25C_n^2L^3W_0^{-\frac{1}{3}} \int_0^1 \xi^2 \left(\frac{1}{((\Theta_0 + \bar{\Theta}_0\xi)^2 + 1.63\sigma_R^{\frac{12}{5}}\Lambda_0(1-\xi)^{\frac{16}{5}})^{\frac{1}{6}}} \frac{(\kappa_0W_0)^{\frac{1}{3}}}{(1 + \kappa_0^2W_0^2((\Theta_0 + \bar{\Theta}_0\xi)^2 + 1.63\sigma_R^{\frac{12}{5}}\Lambda_0(1-\xi)^{\frac{16}{5}}))^{\frac{1}{6}}} \right) d\xi. \quad (2.71)$$

Scintillations

For the sake of completeness, it should be mentioned that, same as under weak conditions, the Scintillation index is also split up under strong fluctuations:

$$\sigma_I^2(r, L) = \sigma_{I,r}^2(r, L) + \sigma_{I,l}^2(L). \quad (2.72)$$

The radial component, of an untracked beam, can be calculated as

$$\sigma_{I,r}^2(r, L) \approx 4.42\sigma_R^2\Lambda_e^1\frac{5}{6}\left(\frac{r - \sigma_{pe}}{W_{LT}}\right)^2, \quad \sigma_{pe} \leq r \leq W. \quad (2.73)$$

Here, all variables with the subscript “e” belong to a new set of effective beam variables which are calculated as

$$\begin{aligned} \Theta_e &= \frac{\Theta - 0.81\sigma_R^{\frac{12}{5}}\Lambda}{1 + 1.63\sigma_R^{\frac{12}{5}}\Lambda}, \\ \Lambda_e &= \frac{\Lambda}{1 + 1.63\sigma_R^{\frac{12}{5}}\Lambda}, \\ \bar{\Lambda}_e &= 1 - \Lambda_e, \\ \bar{\Theta}_e &= 1 - \Theta_e. \end{aligned} \quad (2.74)$$

σ_{pe} is the variance of the effective pointing error defined as

$$\sigma_{pe}^2 = 7.25C_n^2L^3W_0^{-\frac{1}{3}} \int_0^1 \xi^2 \left(\frac{1}{|\Theta_0 + \bar{\Theta}_0\xi|^{\frac{1}{3}}} - \left(\frac{\kappa_0^2W_0^2}{1 + \kappa_0^2W_0^2(\Theta_0 + \bar{\Theta}_0)^2} \right)^{\frac{1}{6}} \right) d\xi. \quad (2.75)$$

The longitudinal component of the scintillation index is defined as

$$\sigma_{I,l}^2(L) = e^{\frac{0.49\sigma_B^2}{(1+0.56(1+\Theta)\sigma_B^{\frac{12}{5}})^{\frac{7}{6}}} + \frac{0.51\sigma_B^2}{(1+0.69\sigma_B^{\frac{12}{5}})^{\frac{5}{6}}}}, \quad (2.76)$$

where σ_B^2 is the Rytov variance of a beam wave

$$\sigma_B^2(L) \approx 3.86\sigma_R^2(0.4((1 + 2\Theta)^2 + 4\Lambda^2)^{\frac{5}{12}} \cos\left(\frac{5}{6} \arctan\left(\frac{1 + 2\Theta}{2\Lambda}\right)\right) - \frac{11}{16}\Lambda^{\frac{5}{6}}). \quad (2.77)$$

2.5.3 Scintillation Simulation beyond W

In a recent paper of Andrews and Phillips [4], some graphs show a simulation beyond W . These graphs show the well known analytical quadratic increase of the scintillation index as well as a simulation beyond this point for two different cases. It can be seen that the increase of the scintillation index is not as steep as the theory predicts. The maximum can be estimated as a little bit less or roughly equal to two times the beam radius. The decrease beyond this maximum and the interesting behavior after the decrease was not simulated or shown in this graph. The maximal scintillation index is around 2.5 to 2.8 times the scintillation index at the beam radius W .

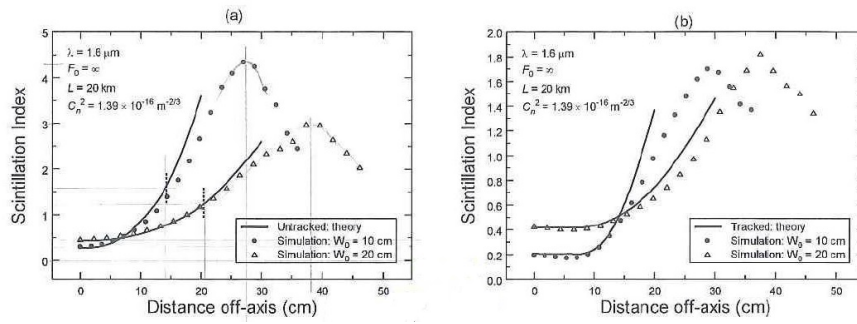


Figure 2.6: Scintillation index off-axis (simulation). Source: [4]

Chapter 3

Measuring Principles

3.1 Cassegrain Telescope

The Cassegrain reflector is a mirror telescope invented by Laurent Cassegrain in the 17th century shortly after the invention of the Newtonian telescope by Sir Isaac Newton. It consists of a tube and a primary and secondary mirror. The primary mirror is of parabolic shape with the concave side to the opening of the telescope. The secondary mirror is of hyperbolic shape with the convex side facing the primary mirror.

Light entering the telescope on or parallel to the optical axis is reflected on the primary mirror to the focus point of the paraboloid. The secondary hyperbolic mirror has two focus points. When a beam is propagating to the focus point of the other side of the mirror, it is reflected to the focus point on the same side of the mirror. In the Cassegrain telescope, the focus point of a parabolic primary mirror and the concave focus point of the hyperbolic secondary mirror are equal. This way, light reflected from the primary mirror is reflected on the secondary mirror and from there is reflected to the convex focus point of the secondary mirror. The convex focal point

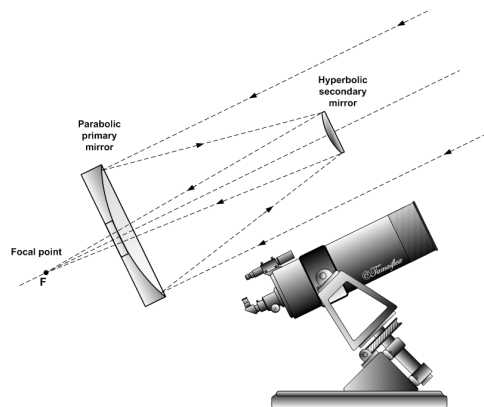


Figure 3.1: Principle of a Cassegrain telescope. Source: [5].

can be located in front or behind the primary mirror. If it is located behind the primary mirror, the mirror acts as a circular opening. On small Cassegrain telescopes, the secondary mirror is held by a transparent plate that seals off the tube. On larger telescopes, there is a spider holding

the mirror. This results in two different effects of shadowing, one from the secondary mirror and one from the spider holding the secondary mirror. Due to the secondary mirror, the focal length of the telescope is enlarged and a more compact design is possible.

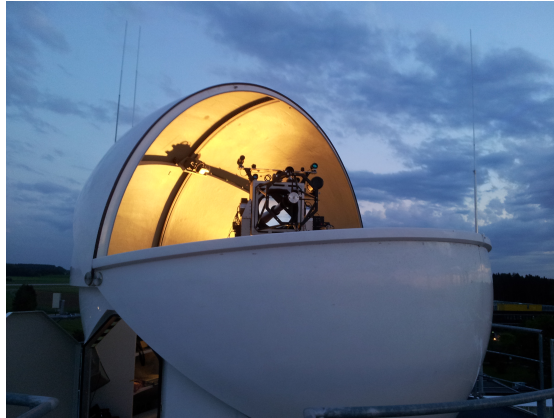


Figure 3.2: Picture of the Cassegrain telescope at the measuring site.

3.2 Collimator

Collimators are used to parallelize a beam or focus a parallel beam to a point. The simplest construction of a collimator consist of a tube with a mounting point for the source or receiver in the appropriate distance to the lens in the collimator. As discussed in section 2.4, it is not possible to get a parallel, not-broadened Gaussian wave.

In this section, only the case of paralleling a beam is discussed. If the distance between the lens and the source is varied, three different types of beams are possible. If the source, or, more precisely, the point source substitution is exactly equal to the focal length from the lens, the beam is collimated. If the source is moved further away, the beam gets focused. If it is moved closer to the lens, the beam is getting divergent.

Collimators are characterized by their beam divergence angle and the beam diameter. The product of these two values is a constant. If a lower angle is necessary, this results in a larger beam diameter. The beam diameter can be characterized in many different ways. One commonly used is the full width at half maximum (FWHM). In this case, the diameter is defined as the distance between the two points where the intensity is reduced to half the maximum intensity. In another definition, the point where the intensity reaches $\frac{1}{e^2}$ is taken as the measuring point. If the beam form is known, the two definitions can be converted.

3.3 Shearing Interferometer

A shearing interferometer is a simple interferometer used to check whether a beam is collimated. It consist of just an optical glass with two slightly angled, extremely flat surfaces. This glass is placed under an angle of 45° in the propagation path. When the beam hits the plate, there are two reflections on the front and the back side of the glass, as shown in 3.4. These two reflected beams create an interference pattern in the overlapping area. This pattern looks like equally spaced fringes and rotates according to the radius of curvature. If the beam is collimated at this

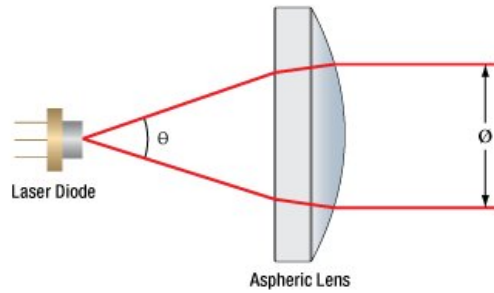


Figure 3.3: Principle of a collimator. Source: [6].

point – i.e., if the beam waist is located at the position of the shear-plate – the fringes should be parallel to the beam propagation path. If the beam is divergent or focused, the fringes are rotated either clockwise or counterclockwise.

3.4 InGaAs Camera

InGaAs detectors are semiconductors sensitive in the near-infrared region. This is due to their direct band gap around 0.5 eV, depending on the relative concentrations of Indium and Gallium. The effect responsible for the sensitivity of InGaAs is the inner photoelectric effect. If a photon with higher energy than the band gap is absorbed by the semiconductor, it creates an electron-hole-pair, leading to a current. One advantage of InGaAs is that the cutoff wavelength can be set by the proportion of Indium and Gallium. Another advantages of this type is that it can be operated at room temperature and the output is almost linearly proportional to the irradiance.

For the experiments described in the thesis at hand, a Xenics InGaAs-camera was used. This camera was controlled by a handmade software running on a PC next to the telescope. The camera can be toggled between high gain and low gain and the integration time of a picture can be adjusted. The camera software has two different modes. One mode is the live view mode, where everything happening on the telescope can be monitored live, but no pictures can be captured. The second mode is the sequence mode, where certain number of frames can be captured by the camera and saved on the PC. While operating in this mode, only a few frames grabbed from the camera can be seen in a given period of time, which results in a slow fps of the primary mirror picture on the screen. When a pixel on the screen is white, it indicates that the pixel on camera is saturated and the integration time should be decreased.

3.5 Laser

Lasers in the near infrared region, including 1550 nm, are typically semiconductor lasers. All semiconductor laser use the same principle. The wavelength is varied by the applied semiconductor material.

The basic mechanism that leads to emission of light is the recombination of holes and electrons in the semiconductor. This environment is created by driving a p-n junction in forward bias. This creates an essential population inversion. The optical resonator is bordered by the edge of the semiconductor because of the change of refraction index or by some additional coatings. The energy conversion efficiency of laser is bad in general, but is quite good with roughly 70% in the IR-region. Because of the small size of the active zone, one of the main problems is the heat loss,

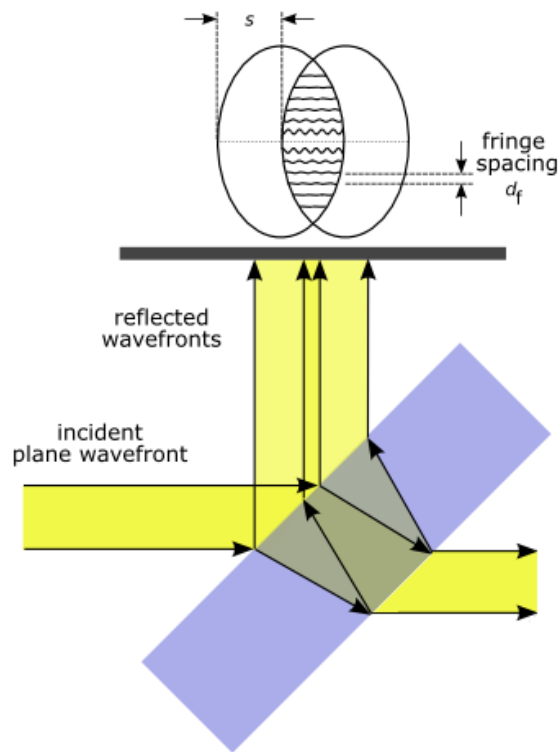


Figure 3.4: Principle of a shearing interferometer. Source:[7].

which gets more critical with higher laser power.

Security considerations have to be regarded depending on the wavelength and output power of the laser. Infrared lasers pose an additional thread, as the emitted light is invisible for human eyes, but can burn the retina.

3.6 Requirements

The project required measurements of the off-axis scintillations at an off-axis distance of two to three times the beam radius using a 40 cm telescope and a roughly 750 m test link at two different beam divergences. The measurements had to be done on different days in order to handle different C_n^2 .

3.7 Design

In a first setup, a 40 cm Cassegrain reflector was used. Due to its secondary mirror and the four spiders holding it, only one quarter of the primary mirror can be used. A test track of 750 m distance between two DLR buildings was used. The wavelength of the laser was determined to

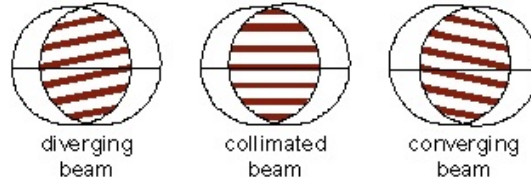


Figure 3.5: Orientation of the fringes dependent on the beam characteristic Source: [8].

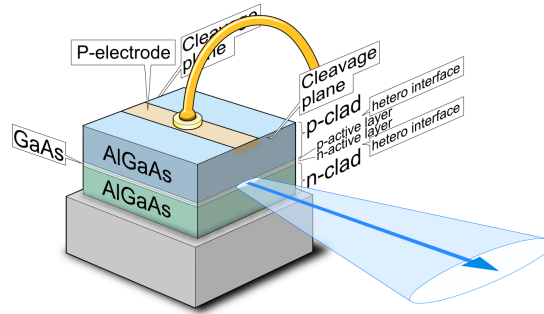


Figure 3.6: Principle of a laser diode. Source: [9].

be 1550 nm. A collimated beam was used to try to and measure 3W away from the beam center:

$$\begin{aligned}
 W_0 &= 0.0035 \text{ m} \\
 L &= 750 \text{ m} \\
 \lambda &= 1550 \text{ nm} \\
 C_n^2 &= 10^{-13} \text{ m}^{-2/3} \text{ to } 10^{-14} \text{ m}^{-2/3} \\
 \alpha &= -2 \times 10^{-5} \\
 F_0 &= \infty,
 \end{aligned} \tag{3.1}$$

$$k = \frac{2\pi}{\lambda}. \tag{3.2}$$

The divergency of a diffraction limited Gaussian beam is calculated as

$$\theta = \arctan \frac{\lambda}{\pi W_0}. \tag{3.3}$$

The following propagation parameters are needed to calculate the transmission through the atmosphere:

$$\Lambda_0 = \frac{2z}{kW_0^2} \tag{3.4}$$

$$\Theta_0 = 1 - \frac{z}{F_0} \tag{3.5}$$

$$\Lambda = \frac{\Lambda_0}{\Theta_0^2 + \Lambda_0^2} \tag{3.6}$$



Figure 3.7: Aerial view of the test link site.

$$\Theta = \frac{\Theta_0}{\Theta_0^2 + \Lambda_0^2}. \quad (3.7)$$

The width of the irradiation distribution after the propagation in absence of any turbulence is W :

$$W = W_0 \sqrt{\Theta_0^2 + \Lambda_0^2}. \quad (3.8)$$

The Rytov variance (σ_R^2) is defined as

$$\sigma_R^2 = 1.23 C_n^2 k^{7/6} L^{11/6}. \quad (3.9)$$

If one of these two conditions is violated, the turbulence is considered moderate to strong or strong:

$$\begin{aligned} \sigma_R^2 &< 1 \\ \sigma_R^2 \Lambda^{5/6} &< 1. \end{aligned} \quad (3.10)$$

For the estimated C_n^2 , a σ_R^2 from 0.1175 to 1.175 was measured. As a consequence, it was necessary to calculate the propagation for strong turbulence.

Due to refraction effects in the atmosphere, the instantaneous Gaussian distribution is moving over time. This so called beam wander results in a long term distribution of the irradiation. If the spatial coherence radii of the corresponding plane satisfy $\rho_{pl} \gg l_0$, it can be concluded that

$$\rho_{pl} = (1.46 C_n^2 k^2 L)^{-\frac{3}{5}}, \quad C_n^2 = \text{const.} \quad (3.11)$$

and

$$W_{LT} = W \sqrt{1 + 1.63 \sigma_R^{\frac{12}{5}} \Lambda}. \quad (3.12)$$

For further calculations, the tracked on-axis scintillations of the first order Rytov theory σ_B^2 is required as well as the effective beam parameter Λ_e :

$$\sigma_B^2 = 3.86 \sigma_R^2 (0.4[(1 + 2\Theta)^2 + 4\Lambda^2]^{\frac{5}{12}} \cos(\frac{5}{6} \arctan(\frac{1 + 2\Theta}{2\Lambda})) - \frac{11}{16} \Lambda^{\frac{5}{6}}), \quad (3.13)$$

$$\Lambda_e = \frac{2L}{kW_{LT}^2}. \quad (3.14)$$

From the above equations, the on- and off-axis scintillations for strong turbulence can be calculated:

$$\sigma_{\text{on}} = e^{\frac{0.49\sigma_B^2}{(1+0.56(1+\Theta)\sigma_B^{\frac{12}{5}})^{\frac{7}{6}}} + \frac{0.51\sigma_b^2}{1+(0.69\sigma_B^{\frac{12}{5}})^{\frac{5}{6}}}} \quad (3.15)$$

and

$$\sigma_{\text{off}} = 4.42\sigma_R^2 \Lambda_e^{\frac{5}{6}} \frac{r^2}{W_{LT}}, \quad r < W. \quad (3.16)$$

3.8 Realization

3.8.1 Large Divergence

The initial parameters for the collimator with large divergence are:

$$\begin{aligned} W_0 &= 3.5 \text{ mm} \\ C_n^2 &= 1 \times 10^{-13} \text{ m}^{-2/3} \\ L &= 735 \text{ m} \\ \lambda &= 1550 \text{ nm}. \end{aligned} \quad (3.17)$$

A collimated beam was used and then the divergence angle and the free space spot size was calculated as

$$\begin{aligned} \theta &= 141 \text{ mrad} \\ W &= 10.37 \text{ cm}. \end{aligned} \quad (3.18)$$

After this, the Rytov variance is

$$\begin{aligned} \sigma_R^2 &= 1.1322 \\ \sigma_R^2 \cdot \Lambda_e^{\frac{5}{6}} &= 0.0672. \end{aligned} \quad (3.19)$$

In the given case, the turbulence has to be considered moderate to strong. The long term spot size is calculated as

$$W_{LT} = 10.82 \text{ cm}. \quad (3.20)$$

With all the previous calculations, the on-axis scintillation and the off-axis scintillations can be deduced as

$$\begin{aligned} \sigma_{\text{on}}^2 &= 0.3623 \\ \sigma_{\text{off}}^2 &= 23.628 \cdot r^2. \end{aligned} \quad (3.21)$$

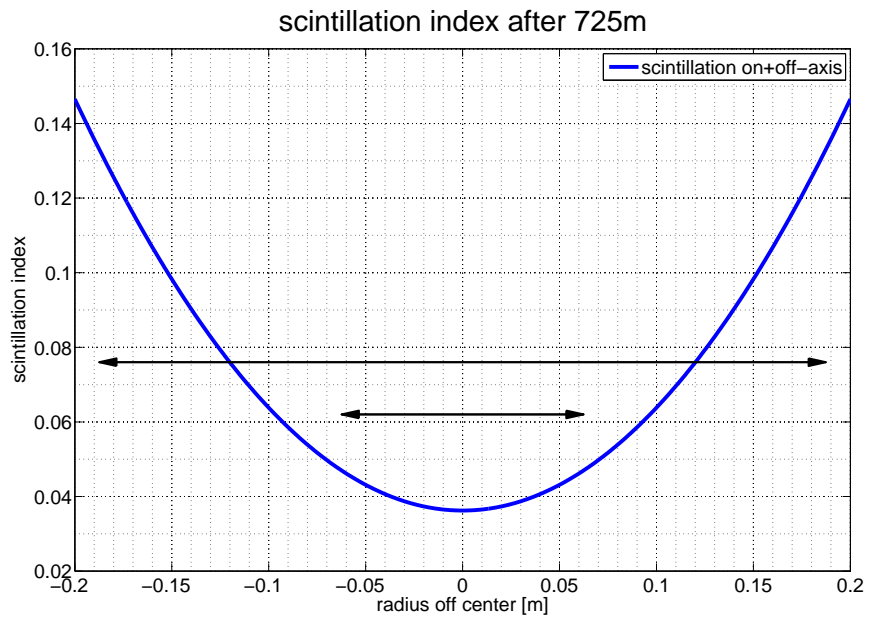


Figure 3.8: Rough estimation of the Scintillation index for a collimator with large divergence. The short arrow marks $\pm W_{LT}$, whereas the long arrow marks $\pm 3 \cdot W_{LT}$.

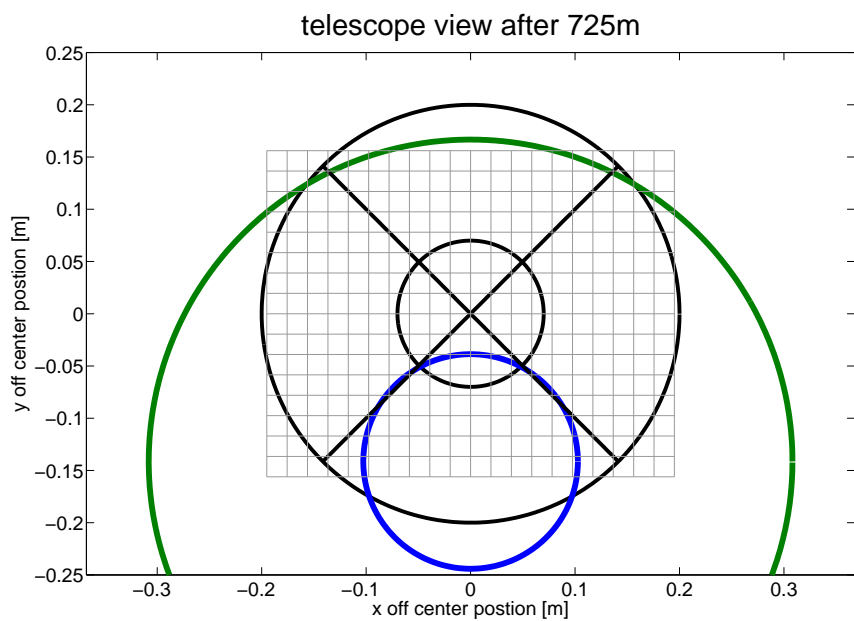


Figure 3.9: View of the telescope (black rings). The blue ring shows the beam at W_{LT} and the green ring shows $3W_{LT}$.

3.8.2 Small Divergence

This is the same calculation as in the section above using the other collimator. The initial parameters for the collimator with the small divergence are:

$$\begin{aligned}W_0 &= 9.4 \text{ mm} \\C_n^2 &= 1 \times 10^{-13} \text{ m}^{-2/3} \\L &= 735 \text{ m} \\ \lambda &= 1550 \text{ nm}.\end{aligned}\tag{3.22}$$

Using a collimated beam, the divergence angle and the free space spot size can be calculated as

$$\begin{aligned}\theta &= 52 \text{ mrad} \\W &= 3.96 \text{ cm}.\end{aligned}\tag{3.23}$$

The Rytov variance is

$$\begin{aligned}\sigma_R^2 &= 1.1322 \\ \sigma_R^2 \cdot \Lambda^{\frac{5}{6}} &= 0.3341.\end{aligned}\tag{3.24}$$

Again, the turbulence has to be considered moderate to strong. The long term spot size is calculated as

$$W_{LT} = 4.76 \text{ cm}.\tag{3.25}$$

Concluding, the on- and off-axis scintillation are

$$\begin{aligned}\sigma_{\text{on}}^2 &= 0.2498 \\ \sigma_{\text{off}}^2 &= 479.982 \cdot r^2.\end{aligned}\tag{3.26}$$

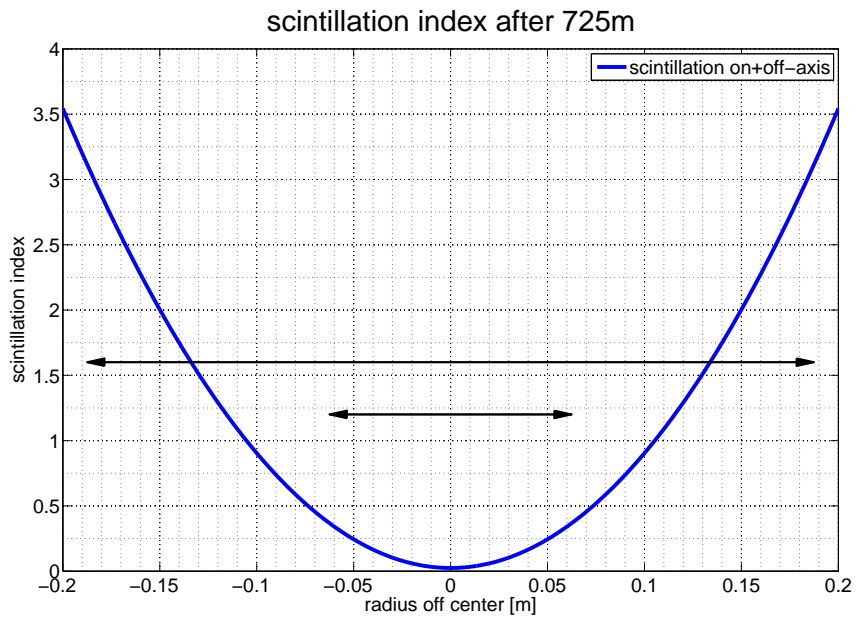


Figure 3.10: Rough estimation of the Scintillation index for a collimator with small divergence. The short arrow marks $\pm W_{LT}$, whereas the long arrow marks $\pm 3 \cdot W_{LT}$.

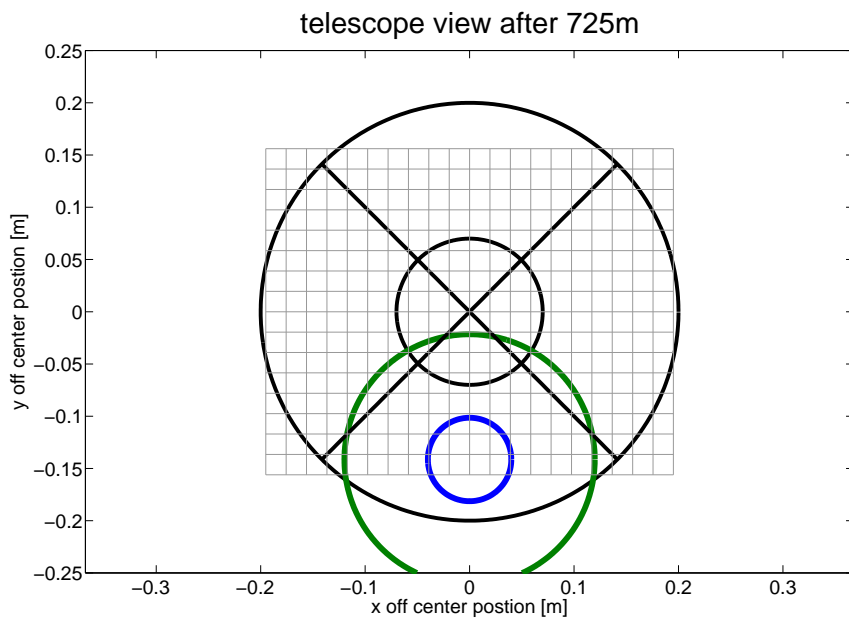


Figure 3.11: View of the telescope (black rings). The blue ring shows the beam at W_{LT} and the green ring shows $3W_{LT}$.

Chapter 4

Preliminary Setup

In the preliminary setup, only one divergence (i.e., one collimator) was used to see if basic problems would occur.

4.1 Tilt Rotation Platform

To simplify the alignment of the collimator, a tilt rotation stage was used to independently move the x-axis and the y-axis on the mirror of the telescope. The main requirement for this platform was its maneuverability in adequately small steps, so that the beam could be well positioned on the primary mirror of the telescope. A rotation stage from Newport was used for this function. The stage was modified with new micrometer screws to achieve the necessary resolution. The new



Figure 4.1: Newport stage. Source: [10].

resolution on the primary mirror could easily be calculated. The distance between the support point of the upper plate and the screws is 45 mm and 60 mm, respectively, and the minimal step size of the micrometer screw is $0.5\ \mu\text{m}$. With the intercept theorem we can thus calculate the

accuracy of the beam adjustment as

$$\frac{\text{support point} - \text{screw}}{\text{support point} - \text{telescope}} = \frac{\text{resolution screw}}{\text{resolution telescope}} \quad (4.1)$$
$$\text{resolution telescope} = 0.0005 \text{ mm} \cdot \frac{750 \text{ m}}{45 \text{ mm}} \approx 8 \text{ mm}.$$

4.2 Testlink and Alignment

A distance over 750 m was implemented between the telescope on the roof and a nearby building. On this building, a 19-inch rack was installed with a power supply and an IR source with a wavelength of 1550 nm. The collimator on the tilt rotation platform was mounted into this rack and connected to the 1 mW source with a single mode fiber. The alignment of the collimator was done by a scope that was placed on top to get a vertical alignment and was placed on the side of the collimator to align it horizontally. After the collimator had been aligned in this way, the beam was moved around the initial position until the source was visible on the wide field of view camera. This camera is placed on the top of the telescope and helps guiding the beam on the primary mirror. Once the beam is visible on the wide field of view camera, it is adjusted so that the bright speckle on the camera screen gets as big as possible. After doing this, it is necessary to increase the integration time of the camera until speckles appear on the primary mirror. Subsequently, the beam needs to be guided to the correct location on the mirror. When the center of the beam approaches the mirror, the camera will most probably be saturated at one point. When this is the case, the integration time needs to be reduced so that a clearer picture of the beam center can be achieved. When the beam center is in the middle of a quadrant of the primary mirror, the measurement can be taken.

4.3 Measurement

If a picture is taken by the camera, there is background noise and background radiation. It is advisable to switch on the camera half an hour before using it in order to reduce the unstable noise of the camera after switching it on. The noise and the background radiation vary with the integration time, so there needs to be an unilluminated picture for every integration time. In the first run, 5000 pictures were taken with the source switched on and 300 pictures without a source.

Due to the dynamic range of the camera, the beam must be scanned in pieces with different integration times and must be put together afterward to get the whole beam profile. Therefore, the integration time was varied according to table 4.3. After these measurements, a second source with a very wide beam was used to illuminate the whole primary mirror homogeneously. In this setup, another 5000 frames were taken. These completely illuminated pictures were taken in order to simplify the post processing phase by finding the shape of the primary mirror from this broad beam rather than from the very small one.

4.4 Problems

During the measurements and the post processing of the measurements, several problems occurred.

Camera settings	
gain	integration time [μs]
low	1
low	2
low	4
low	8
low	16
low	32
low	64
low	128
low	256
low	512
low	1024
low	2048

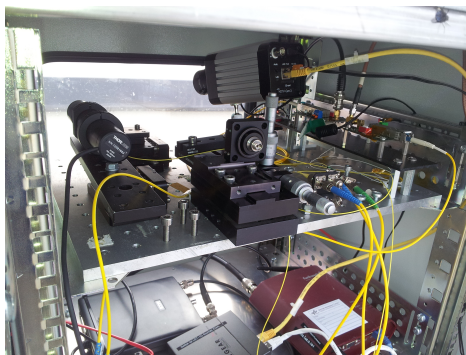


Figure 4.2: Collimator mounted on the stage in the rack.

4.4.1 Rubber Floor Plate

The position of the beam was very unstable so that during the measurements it was quite hard to even position the beam more or less exactly where it should be. Besides this, the beam was moving in such large scales after positioning that a different origin other than mere beam wandering had to be suspected. It was found that there was predominant direction movement correlated with flurries hitting the rack. This was overlaid by more or less random movements correlated with the movements of the person adjusting the beam. These problems originated from the installation of the rack on the roof. As seen in fig. 4.3, the whole roof was covered by a 1 cm to 2 cm thick rubber plate to prevent the water sealing layer underneath it from damage. This rubber plate was covered by a layer of broken stones. When the rack was installed on the roof, the broken stones were removed and the rack was placed on alloy plates directly lying on the rubber layer. After discovering this hindrance, it was decided that the rack was an unsuitable place to mount the collimator.

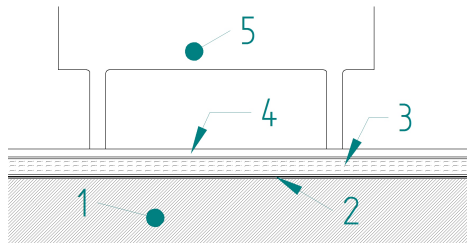


Figure 4.3: 1.concrete roof; 2.bitumen water sealing; 3.rubber plates layer; 4.alloy plate; 5.19-inch rack.



Figure 4.4: Rack standing on alloy plates laying on the rubber layer of the roof.

4.4.2 Small Magnification

The camera used has a resolution of 256 x 320 pixel and was already installed in an optical setup behind the telescope so that the compression factor and hence the magnification were fixed.

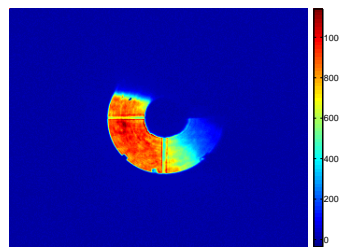


Figure 4.5: The whole picture represents the sensor area of the camera. The small magnification means bad usage of this area.

To get a finer resolution of the beam profile, it was necessary to increase the magnification. If the beam could be placed very accurately, it would be sufficient even without the entire primary mirror of the telescope being visible on the camera.

4.4.3 Interference Pattern

After analyzing the homogenous illuminated pictures, a lamellar pattern showed up in the scintillation index. To isolate the origin of this effect, a second collimator with a big divergence was used in order to completely illuminate the primary mirror. This second collimator was also placed on top of the box to avoid any effects of the transparent window of the rack. This way, the origin of the pattern was isolated at the optical path behind the telescope. It was not possible to track down or entirely understand the mechanisms that lead to that pattern.

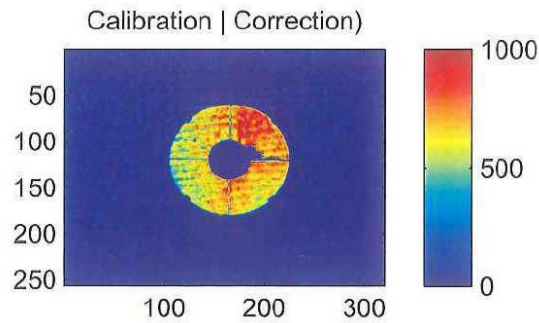


Figure 4.6: Interference pattern.

In order to find a solution to this problem, it was decided to further narrow it down by simplifying the optical path behind the telescope.

4.4.4 Donut Shape

The theory predicts quadratic increases when moving away from the beam center. This behavior was not observed in the first measurements. The problem evolved from a beam shape differing from Gaussian shape. No new insights were achieved by checking the actual collimation of the beam with a shearplate. The beam profile was also checked inside with the benefit of not having to deal with turbulence beyond a distance of 35 m. Beyond this distance, which, other than the test link scenario, can not be considered as far field, no basis for a non-Gaussian beam profile could be found.

To check the beam profile in the far field as well as the collimation, the beam was focused with a lens and the resulting spot was monitored. Because the source could not be tuned in terms of output power, an optical attenuator was used. The applied InGaAs camera was of the same type as the one that was used in the telescope setup. When the integration time was lowered to 1 μ s, the irradiance was too high and the picture was saturated. Just in the middle of the beam there was a spot where the camera could not detect any power at all. When the power was further decreased, the blind spot in the middle vanished and the expected spot could be observed. This behavior of the camera could be explained by a shut down of pixels that receive more than a certain amount of energy, leading to the blind spot in the middle. After further investigating the camera and its behavior at an irradiance higher than the saturation radiation, it was discovered that the value of a pixel follows roughly as shown in the graph below.

The point of beginning decrease varies with the integration time. Because of this critical behavior for small integration times, it was decided to increase integration times over 100 μ s and use an optical attenuator to avoid the critical metering range.

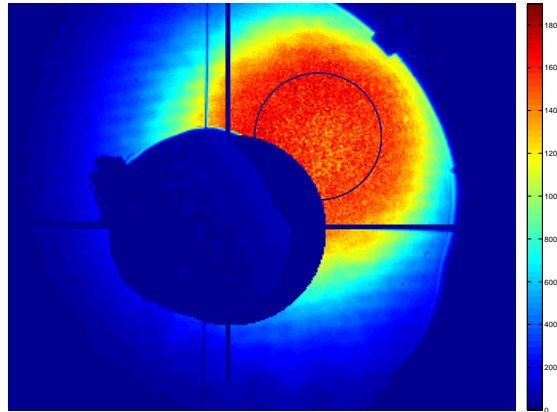


Figure 4.7: Pupil meanfield with the camera problem. In the middle of the beam the intensity is decreasing instead of increasing as would be expected for a Gaussian beam.

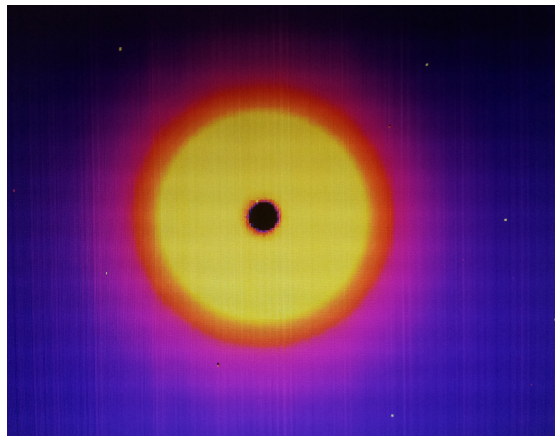


Figure 4.8: Blindspot in the middle of the beam. The small black spot in the middle of the beam shows no intensity at all.

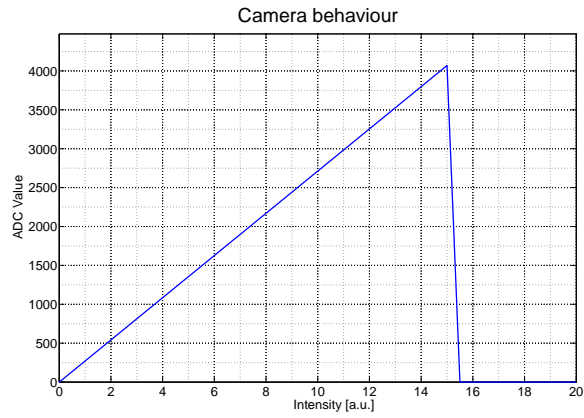


Figure 4.9: Camera behavior. The graph shows the correlation between intensity on the chip of the camera and the converted ADC value, which causes the problem.

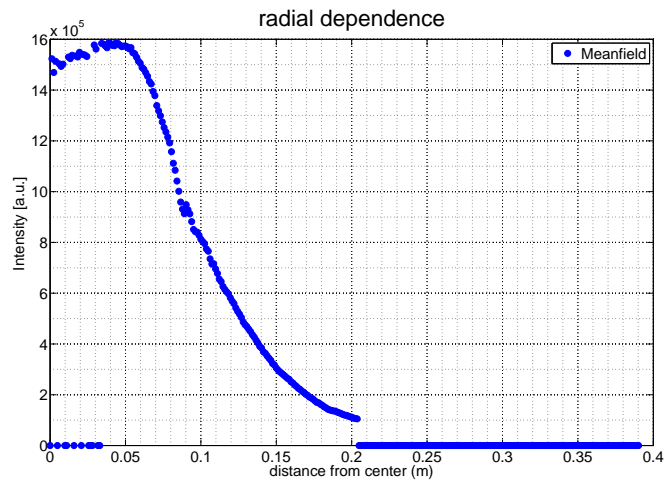


Figure 4.10: Radial meanfield when the camera problem shows up.

4.4.5 Faster Measurements

To hold the C_n^2 more stable over the duration of the measurement, shorter measurement times were required. In a first approach, the necessary number of frames for an integration time measurement was reduced. The possibility for doing so can be investigated by comparing the histogram of certain pixels plotted after 2000, 3000, 4000 and 5000 frames.

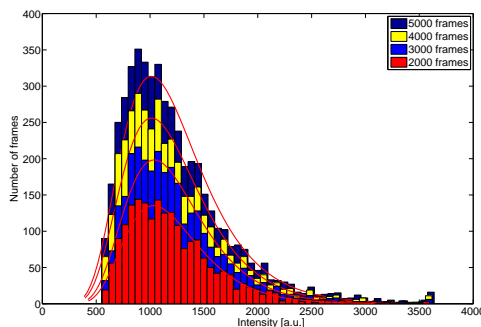


Figure 4.11: Histogram after 5000, 4000, 3000 and 2000 frames. It can clearly be seen that the shape of the distribution is not changing with the number of frames. This shows that 2000 frames are sufficient and additional images provide no additional information.

According to theory, a log-normal distribution is to be expected. In fig. 4.11, it can be seen that the distribution is not changing. This can be easily understood given that they are all normalized to the same value. It can be concluded that more than 2000 frames per integration time do not provide any additional information, but that, on the contrary, they distort the measurement as C_n^2 is not as stable.

A second approach to reduce the measuring time was to avoid starting a second sequence with 300 frames and without a light source. It was found to be faster to take 2500 frames in a row and simply cover the beam after 2000 frames. Although, the additional 200 frames have to be sorted out by doing so, the measuring process itself is faster. The separation between the illuminated and the unilluminated state can be done afterward using a MATLAB script.

The last improvement regarding measurement speed was achieved by not directly connecting the optical attenuators to the collimator, but using a second fiber and mounting the attenuators in between these two fibers.

4.5 Results

By these improvements, measuring off-axis scintillations up to three times the size of the beam radius were possible. It was decided that a collimator with a smaller divergence was required. One exemplary analysis of a measurement is shown in fig. 4.13

In the preliminary setup, no elaborate analysis of the data was done. As seen in fig. 4.12, the mean field of the camera was calculated. This was done by taking into account the back light radiation during the measurement. In fig. 4.13, the corresponding scintillation index of the mean field is presented. In the scintillation index, the interference pattern can clearly be seen. It is worth noticing that a correction of the effect of the interference pattern in the mean field could be quite easily done with a fully illuminated picture. This is not possible with the scintillation index, because a factor of each frame would be shortened out. Despite all these challenges, it

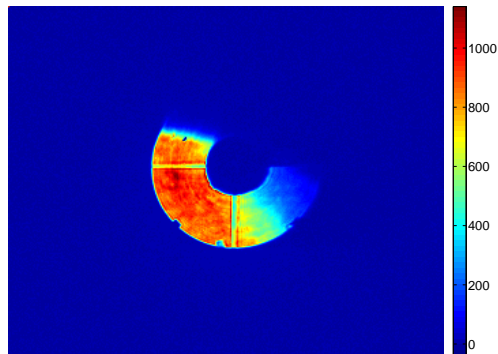


Figure 4.12: Meanfield of a preliminary measurement.

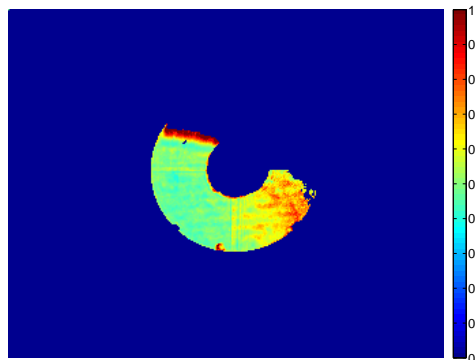


Figure 4.13: Scintillation index of a preliminary measurement.

could be proven that the off-axis scintillation can be measured this way; still, it has to be taken into account that the effort spent on post-processing of the areas with valid information is quite high. To give an example, the spider holding the secondary mirror does not show up as dark lines, as one could expect. This and a number of additional factors need to be taken into account during post-processing of the optimal setup.

Chapter 5

Optimal Setup

With the elucidated changes, successful measurements could be taken.



Figure 5.1: Final setup.

5.1 Improvements

5.1.1 Greater Magnification

The magnification of the telescope setup was increased. To do this and meet the problem of the lamellar pattern, the beam was lifted by a mirror before entering the existing optical setup. The beam was not collimated at this point of the optical setup so that the distance between the last lens and the InGaAs camera could be fixed. Finding the correct distance for the camera to get a sharp picture did not pose an additional challenge. The distance could be varied as long as the shadow of the secondary mirror and the spider holding it was not blurred any further. The new compression achieved this way was ≈ 40 . Because of the magnification being larger by a factor of ≈ 2 , the energy per pixel also decreases by a factor of ≈ 4 .

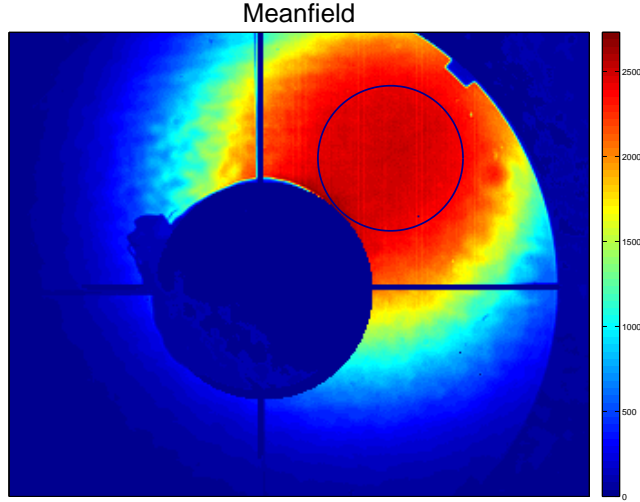


Figure 5.2: Improved big magnification. The area of the camera is far better utilized than before.

5.1.2 New Collimator

To study off-axis scintillations, it was decided in a second scenario to use another collimator. Due to the limitations of the size of the primary mirror, the only possibility was to use a collimator with a smaller beam divergence. No suitable collimator was available, hence a new one needed to be constructed. The following equation can be deduced for the collimation scenario shown in fig. 5.3:

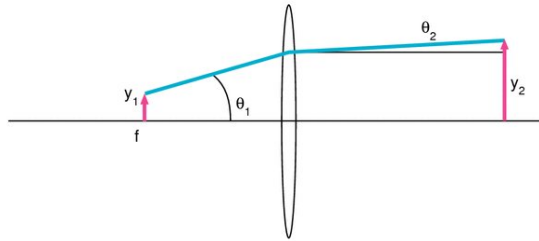


Figure 5.3: Collimation of light from a point. Source: [11]

$$\begin{aligned} y_2 &= \theta_1 \cdot f \\ y_1 &= \theta_2 \cdot f. \end{aligned} \quad (5.1)$$

With these equations and including the approximation for small angles as well the suited characteristics from the fiber, the focal length for the lens of the new collimator was calculated. The required parameters are the core diameter and a numerical aperture of the fiber. With the goal of designing a collimator with a beam diameter around 20 mm, a collimator lens with a focal length of

$$f = \frac{y_2}{\theta_1} = \frac{10 \text{ mm}}{0.095} \approx 106 \text{ mm} \quad (5.2)$$

was necessary. The closest available lens had a focal length of 100 mm. With this selected lens the divergence of the beam will be

$$\theta_2 = \frac{y_1}{f} = \frac{5.25 \text{ } \mu\text{m}}{100} = 52.5 \text{ } \mu\text{rad}, \quad (5.3)$$

which results in a full-angle beam divergence of 105 μrad and a beam diameter of

$$d = 2 \cdot y_2 = \theta_1 \cdot f = 0.095 \cdot 100 \text{ mm} = 19 \text{ mm}. \quad (5.4)$$

5.1.3 Alignment Scope

To enable and simplify the alignment on the telescope, the existing collimator was aligned with the new collimator. For this purpose, the scope was mounted on the stage. As there was only one scope available, both collimators and the scope needed to be mounted on the tilt rotation stage. This posed the challenge of using as little parts as possible due to weight limit arising from the counter springs of the stage.

After mounting all parts on the stage, all three optical axes needed to be in parallel. This was done by using a red laser source on both collimators and trying to place their dots side by side with a distance according to the distance between the collimators. A distance of 35 m was chosen for this purpose. When the collimators were aligned to each other, the scope was aligned to these two spots according to its position on the stage.

5.1.4 Installation Site and Source

Due to the problems with the 19-inch rack standing on the rubber plates, the installation site was moved next to the wall surrounding the roof of the building. As it was not possible to mount the stage directly on the wall, the stage was clamped to an iron bar securing a breakthrough of the wall. Because the new site was a few meters away from the old one, a new source had to be installed. To counteract the loss of irradiance by the greater magnification, a 2 mW IR-source was implemented. Due to the new position, the telescope had to be aligned to the new position as well.

5.2 Measurement

To face the challenges of the camera linked to high radiation and small integration times, optical attenuators were used and therefore an new table of integration times had to developed.

In the new measurement, 2500 frames per integration time were taken and the beam was covered shortly after reaching 2000 frames. A distinction between illuminated and unilluminated pictures was made using a MATLAB script. Under these circumstances, the measurement for the collimator took around xx, excluding the initial alignment. With the simplification linked to the usage of the scope, the alignment itself did not pose any additional challenge. If the scope was aimed at the telescope, the beam was aimed directly at the primary mirror by slightly circling around the telescope. The measurements were taken on three different days to get measurements with different C_n^2 .

Camera settings				
gain	old integration time [μs]	attenuation [db]	calculated equivalent integration time [μs]	integration time [μs]
low	0.25	30	250	250
low	0.5	25	158.1	150
low	1	25	316.2	300
low	1.5	20	150	150
low	2	20	200	200
low	4	20	400	400
low	8	15	253	250
low	16	10	160	160
low	32	10	320	320
low	64	5	202.4	200
low	128	0	128	128
low	256	0	256	256
low	512	0	512	512

Table 5.1: Camera settings for the low divergence collimator.

Camera settings				
gain	old integration time [μs]	attenuation [db]	calculated equivalent integration time [μs]	integration time [μs]
low	0.5	25	158.1	150
low	1	25	316.2	300
low	1.5	20	150	150
low	2	20	200	200
low	4	20	400	400
low	8	15	253	250
low	16	10	160	160
low	32	10	320	320
low	64	5	202.4	200
low	128	0	128	128
low	256	0	256	256
low	512	0	512	512

Table 5.2: Camera settings for the high divergence collimator.



Figure 5.4: Aiming through the scope to place the beam on the primary telescope mirror.

5.3 Post Processing

The post processing was performed in several steps. The first step consisted in selecting the illuminated frames from the background frames. This was done by a script producing correctly named folders with the respective pictures in it. In a first step, the mean frame and the standard deviation of the background measurement were calculated for the whole plane. The standard deviation is used to check whether any illuminated frames were misplaced in the background folder. If this is not the case, the mean field of each background measurement is saved with the information of the integration time. Subsequently, the mean value of the homogeneously illuminated picture is calculated and also saved. After all preliminaries were processed, the script starts by processing the first folder of the measurements step by step. Initially, the script looks for the integration time of the pictures in the folder and tries to find the according mean background frame produced earlier. It further loads the mean frame of the homogeneously illuminated pictures and thus localizes the area with valid information by creating a pattern frame. Valid information can only be acquired in frames where the value of a pixel in the homogeneously illuminate picture exceeds a certain threshold. This pattern serves as a starting point for identifying the areas of valid data. Subsequently, every frame of the measurement folder is loaded and the correct background for the integration time is subtracted from each frame. The mean field and the scintillation index of one single measurement is calculated. During this

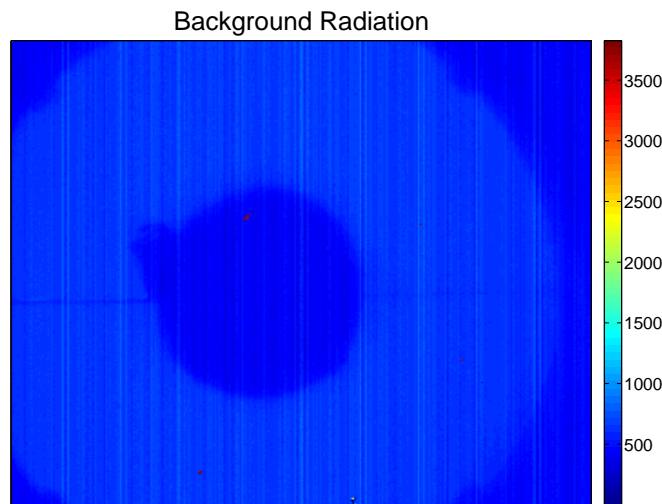


Figure 5.5: Background radiation. This signal is a result of ambient light only.

procedure each pixel is checked for clipping, whereas clipping means that the pixel output has reached its maximum value. Thus, due to the saturation, it is not possible to tell if the pixel shows the true intensity or not. If a pixel has clipped, the information is stored in a single frame. Adding up all the clipping information leads to the following picture. It can be seen that in the middle of the beam where there is too high intensity, all the pixels are clipping. Thus, in this region, there is no valid information to be gained. All pixels clipping more than 10 times are excluded from the area of valid information. When the stack of pictures is processed the center of gravity is computed. This is done by defining a starting point near the center of gravity and by calculating only pixels in a circular region around this point. This is necessary as only a part

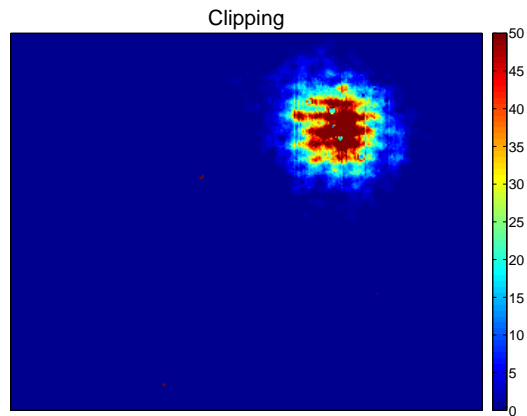


Figure 5.6: Clipping frame. The dark red area shows the position of pixels repeatedly providing no valid data.

of the beam are visible. The part on the primary mirror which is not covered by the secondary beam is captured by the camera. Considering that post processing should also include tracking,

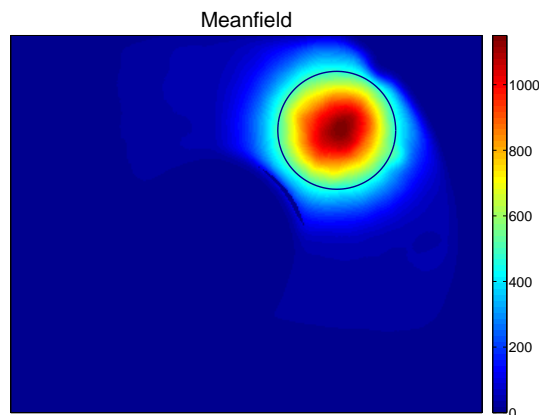


Figure 5.7: Meanfield of the new magnification. The Gaussian distribution of the beam can be seen very clearly.

the mean field needs to be calculated without tracking first to find the exact center of gravity. This center of gravity is now the new starting point for the center of gravity of each frame. The frames are then stitched together with an offset that is the distance between the center of gravity of the mean field and the center of gravity of one frame. If all the positions of the center of gravity of each frame are plotted according to ??, it is possible to observe the beam wander of the experiment. After this step, the spider and everything else – except for the visible part of the primary mirror – is removed manually from the area of valid information. Subsequently, the area of valid information looks like this:

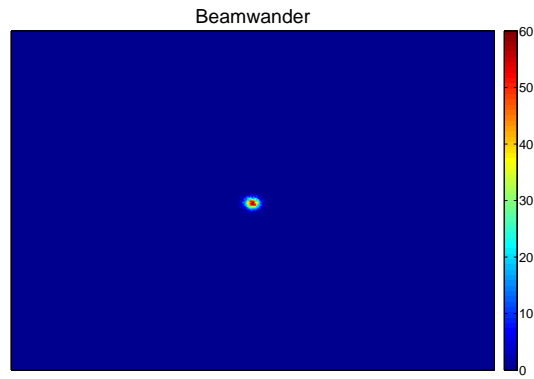


Figure 5.8: Beamwander frame. The closer to yellow or even red a pixel is, the more often the beam center was located at that point in a single frame. Here the distribution of the beam wander can be seen.

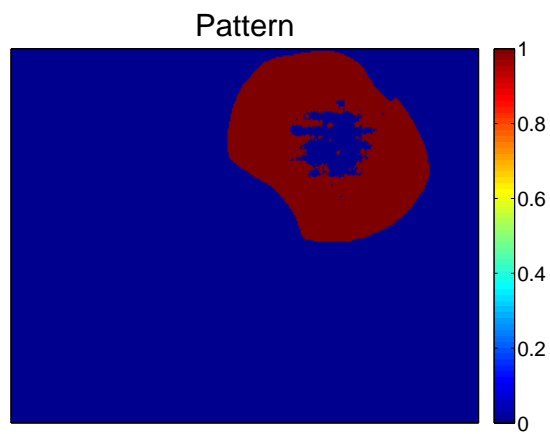


Figure 5.9: Pattern which shows the area of valid data.

And the Scintillation index in this area is calculated like this. This picture is taken and

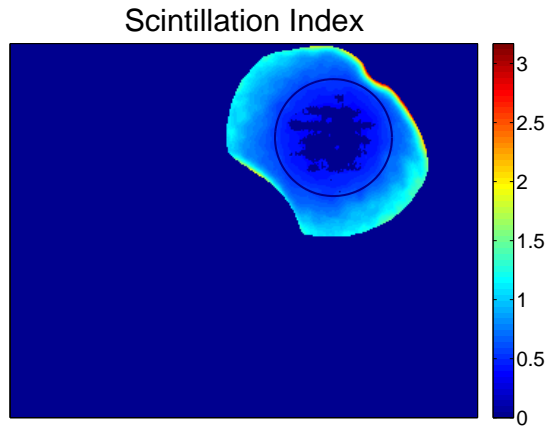


Figure 5.10: Scintillation index. It can be seen that the scintillation index rises away from the center.

circular rings of constant size are placed around the center of gravity. All pixels within a ring are summed up and their mean is calculated. If this mean is plotted over the distance of the ring relative to the center of gravity, the mean field and the scintillation index appear with respect to the off-axis distance. This radially dependent mean field and scintillation index curves are further

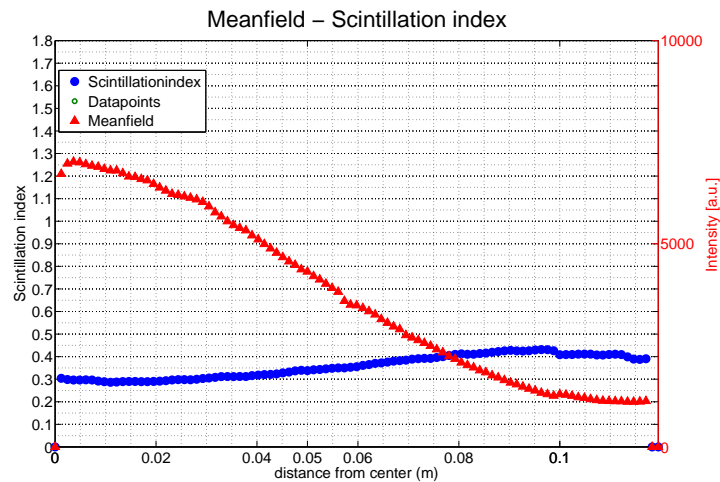


Figure 5.11: Radial dependence of the mean field and the scintillation index for one single integration time of the camera.

processed. First of all, all points which do not rely on an appropriate number of data points are removed. The required number of data points depends on the distance from the center of gravity. In a second step, very basic outlier detection is performed to remove implausible data points. In the present case, this is relatively easy done given that the radial mean field and scintillation

index are known to be smooth functions. If all of the measurements with different integration time for a single collimator are post processed accordingly, they are plotted in graph as shown in fig. 5.12 Subsequently, all different measurements are computed into one. The weighed mean of

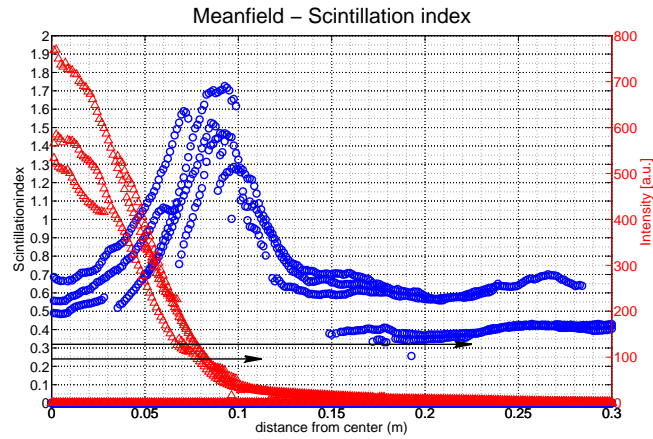


Figure 5.12: Outcome of all radial dependencies of the mean field and Scintillation index plotted at once before they were sticking together. The mean field appears in red and the scintillation index in blue.

this function is calculated using the number of data points as a weighing function. This (fig. 5.13) is basically the essence of each measurement with a single collimator. The function is then split into three parts and fitted with appropriate functions.

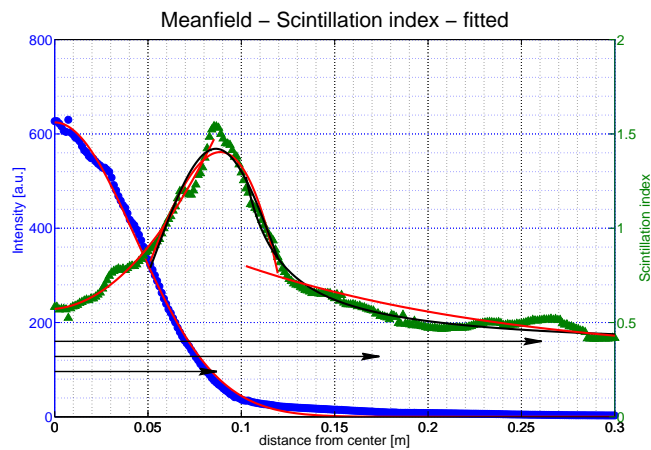


Figure 5.13: Here the radial dependencies of the mean field and the scintillation index after matching of the graphs can be seen. The scintillation index is depicted in green and the mean field in blue.

Chapter 6

Results and Analysis

Three different measurements were taken on three consecutive days. The following analysis is split up into days as the measurements of each day were taken in a short time frame during which, presumably, the turbulence index did not vary significantly. Each analysis of a collimator comes with two sets of evaluation: one untracked, which means that all the frames are simply added up, and one tracked, which, as described earlier, corrects each frame with respect to the center of gravity. The attribute 'big collimator' in this section is used for the physically larger collimator with small divergence and vice versa. It can be seen from the colors of the axis in the following plots that the scintillation index is in green and the mean field blue. The mean field is measured in arbitrary units.

6.1 20.07.2015

The big collimator data is slightly corrupted on the optical axis. This gives an artifact for on-axis scintillation index measurements, which can be neglected. As can be seen in later measurements in agreement with theory, the tracking does not affect the on-axis scintillation index as suggested by the fitting. It is interesting to see that other than the known influences of divergence and tracking on spot size, the off-axis distance of the scintillation index peak does not depend on tracking. Nevertheless, on the big collimator site, the value shows a slight decrease. For the small collimator the effect is harder to isolate as the distribution of the radial scintillation index is not as clear. The off-axis scintillation index apparently reaches a saturation level far off-axis after decreasing. This saturation value lies above the level of the on-axis scintillation index for the big collimator and below this value for the small collimator.

	small untracked	small tracked	big untracked	big tracked
Meanfield				
$\overline{W_{LT}}$	0.082	0.076	0.074	0.07
Scintillationindex				
σ_{on}	0.31	0.31	0.32	0.19
σ_{max}	1.11	1.1	1.41	1.28
$r_{\sigma_{max}} [W_{LT}]$	1.78	1.91	1.18	1.24

Table 6.1: Results for the measurements on 20.07.2015

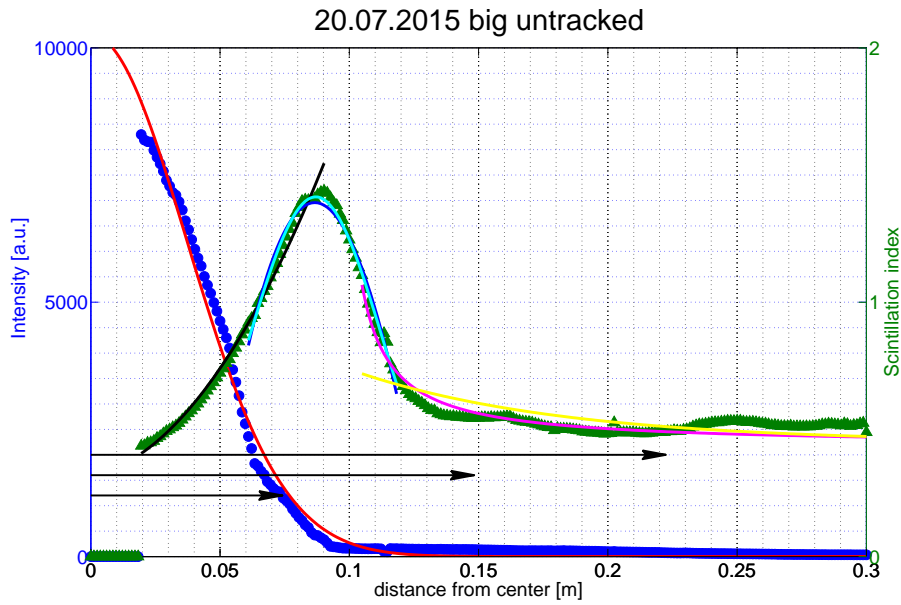


Figure 6.1: Measurement from 20.07.2015 with the small divergence collimator. The arrows point to the single, double and triple beam radius. The mean field can be seen in blue and the Scintillationindex in green.

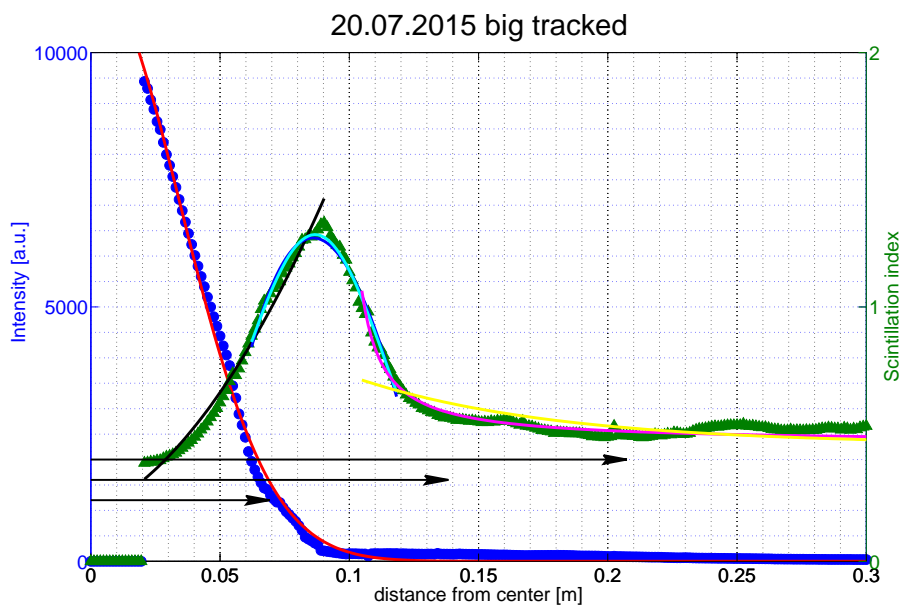


Figure 6.2: Measurement from 20.07.2015 with the small divergence collimator. In the post processing the beam was tracked. The arrows point to the single, double and triple beam radius. The mean field can be seen in blue and the Scintillationindex in green.

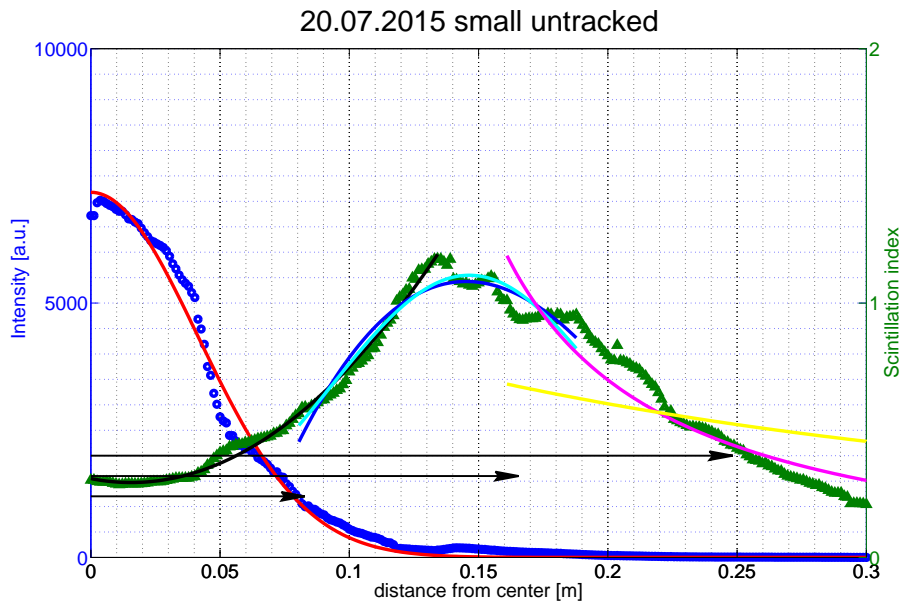


Figure 6.3: Measurement from 20.07.2015 with the big divergence collimator. The arrows point to the single, double and triple beam radius. The mean field can be seen in blue and the Scintillationindex in green.

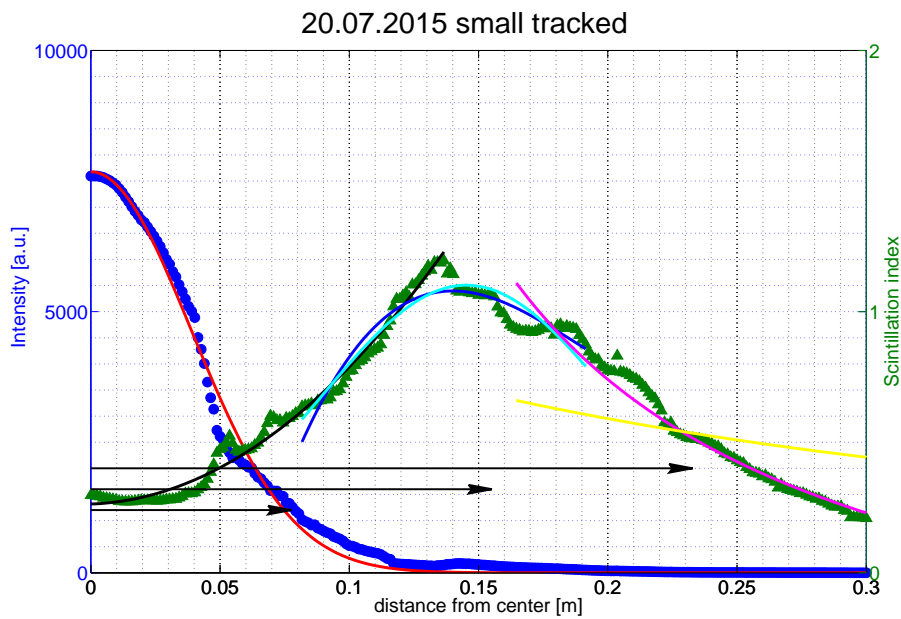


Figure 6.4: Measurement from 20.07.2015 with the big divergence collimator. In the post processing the beam was tracked. The arrows point to the single, double and triple beam radius. The mean field can be seen in blue and the Scintillationindex in green.

6.2 21.07.2015

On 21.07.2015, the on-axis problem with the big collimator was fixed. As can be seen when looking at the range of the scintillation index, the atmosphere on this day was less turbulent than the day before. As a consequence, the scintillation index is roughly just one third of the value measured the day before, thus showing the influence of a very different turbulence index, C_n^2 . As can be seen in the evaluation of the small collimator, the characteristics of the scintillation index deteriorated compared to the previous day. Not even the quadratic increase at the beginning can be seen. The situation could be slightly improved by tracking, but was still unsatisfactory and could not be further improved by post-processing. Thus, the analysis will focus on the data collected with the big collimator. It is interesting to note that again, the off-axis distance corresponding to the maximum scintillation index does not depend on tracking, but stays constant. The maximum scintillation index slightly decreases with tracking. Exactly opposite to the previous measurement, the saturation value far off-axis is lower than the on-axis scintillation index. In addition, the decrease is less steep and the saturation value is reached further off-axis than before.

	small untracked	small tracked	big untracked	big tracked
Meanfield				
$\overline{W_{LT}}$	0.122	0.118	0.078	0.076
Scintillationindex				
σ_{on}	0.12	0.12	0.16	0.15
σ_{max}	0.19	0.2	0.43	0.42
$r_{\sigma_{max}} [W_{LT}]$	0.75	1.18	0.88	0.85

Table 6.2: Results for the measurements on 21.07.2015

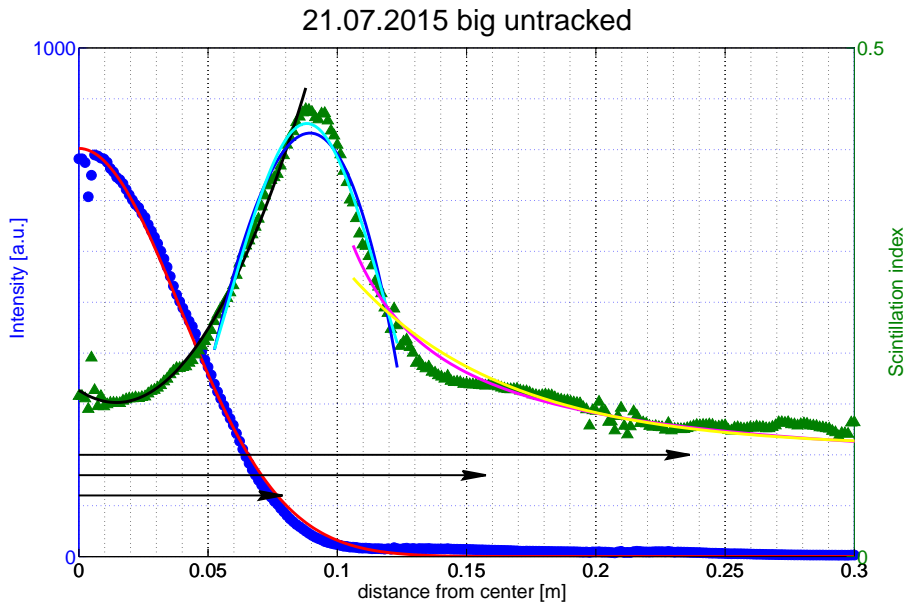


Figure 6.5: Measurement from 21.07.2015 with the small divergence collimator. The arrows point to the single, double and triple beam radius. The mean field can be seen in blue and the Scintillationindex in green.

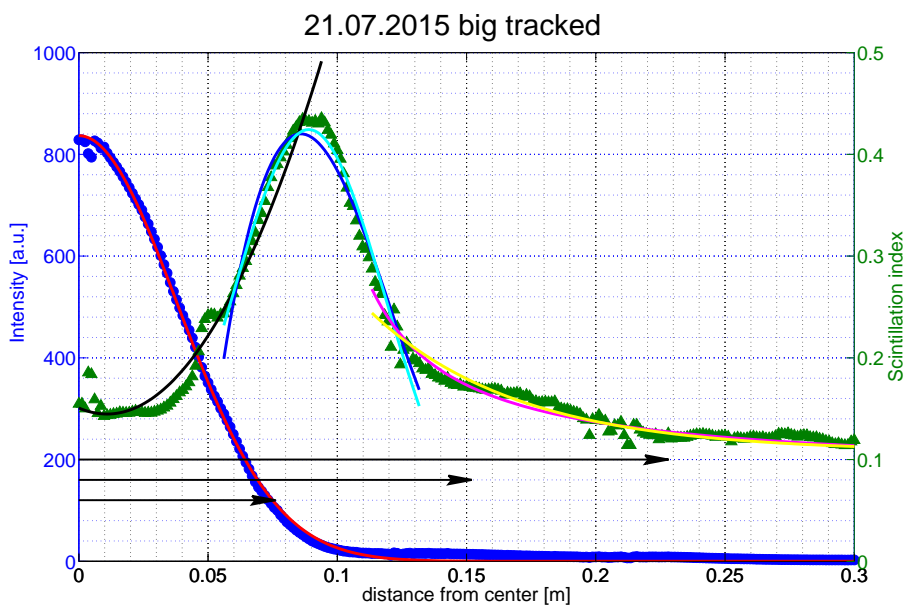


Figure 6.6: Measurement from 21.07.2015 with the small divergence collimator. In the post processing the beam was tracked. The arrows point to the single, double and triple beam radius. The mean field can be seen in blue and the Scintillationindex in green.

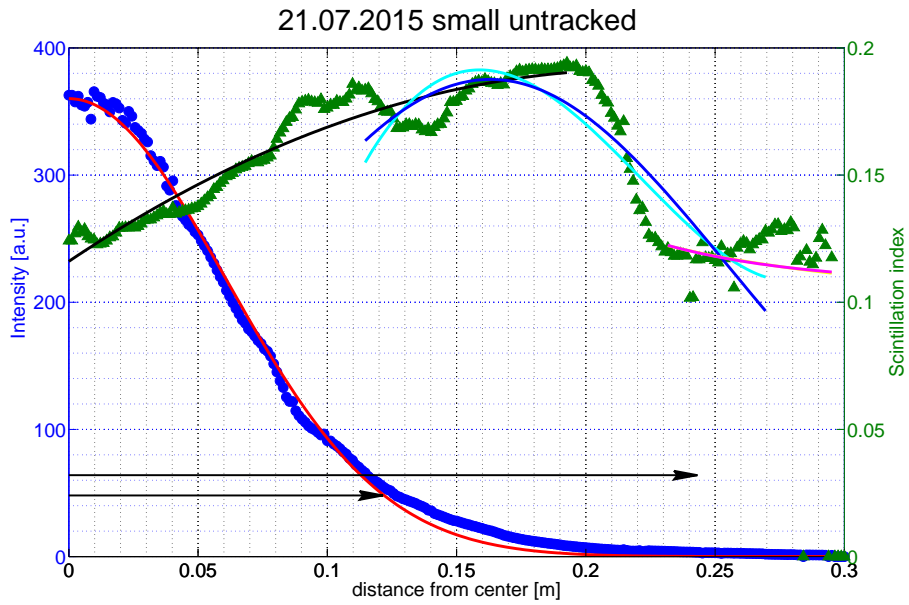


Figure 6.7: Measurement from 21.07.2015 with the big divergence collimator. The arrows point to the single, and double beam radius. The mean field can be seen in blue and the Scintillationindex in green.

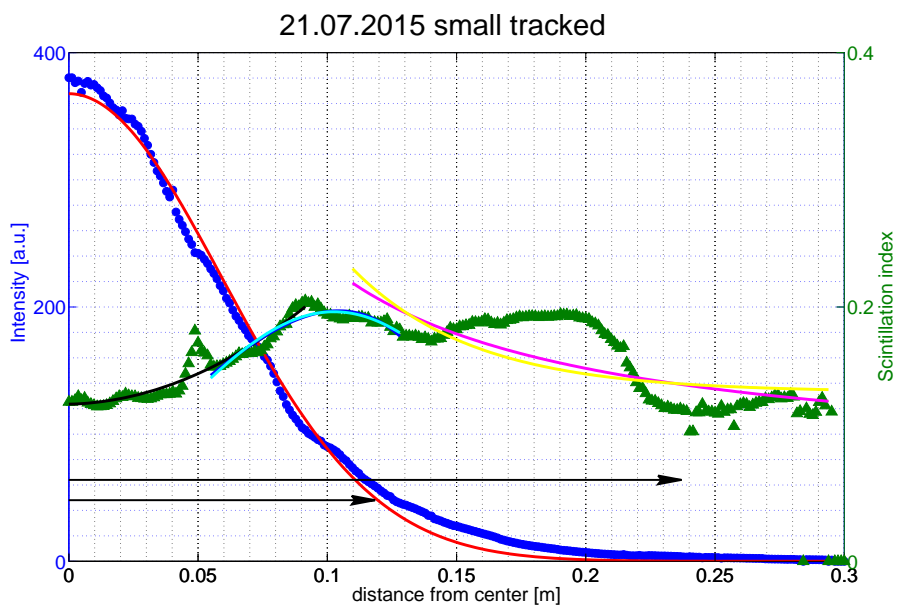


Figure 6.8: Measurement from 21.07.2015 with the big divergence collimator. In the post processing the beam was tracked. The arrows point to the single and double beam radius. The mean field can be seen in blue and the Scintillationindex in green.

6.3 22.07.2015

This measurement was taken on a day with atmospheric turbulence comparable to that of the first day. Consistently, the characteristics of the scintillation index of the big collimator follow the same pattern as before. The small collimator does not show any similarities with the other measurements, which indicates issues with the small collimator which were only visible after post processing. As a consequence, only the measurements using the big collimator are further commented. The maximal scintillation index slightly decreases with tracking of the beam. The scintillation index far off-axis supposedly reaches its saturation value as fast as in the first measurement. Apparently, the saturation value is in the range of the on-axis scintillation index. In good agreement with the previous measurements the radial distance of the scintillation index peak does not depend on tracking.

	small untracked	small tracked	big untracked	big tracked
Meanfield				
W_{LT}	0.11	0.098	0.086	0.074
Scintillationindex				
σ_{on}	0.5	0.45	0.57	0.46
σ_{max}	0.77	0.77	1.42	1.37
$r_{\sigma_{max}}$ [W_{LT}]	1.82	2.04	1	0.86

Table 6.3: Results for the measurements on 22.07.2015

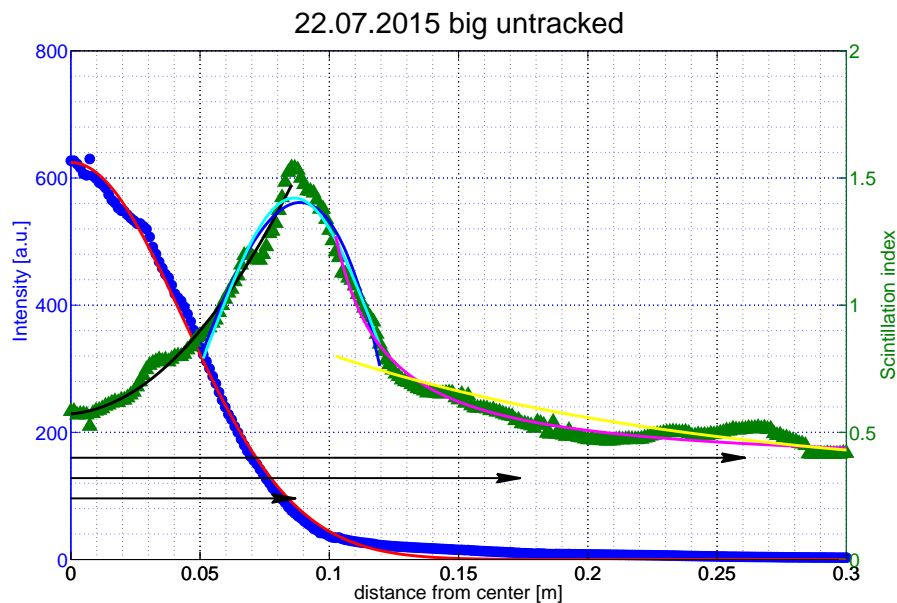


Figure 6.9: Measurement from 20.07.2015 with the small divergence collimator. The arrows point to the single, double and triple beam radius. The mean field can be seen in blue and the Scintillationindex in green.

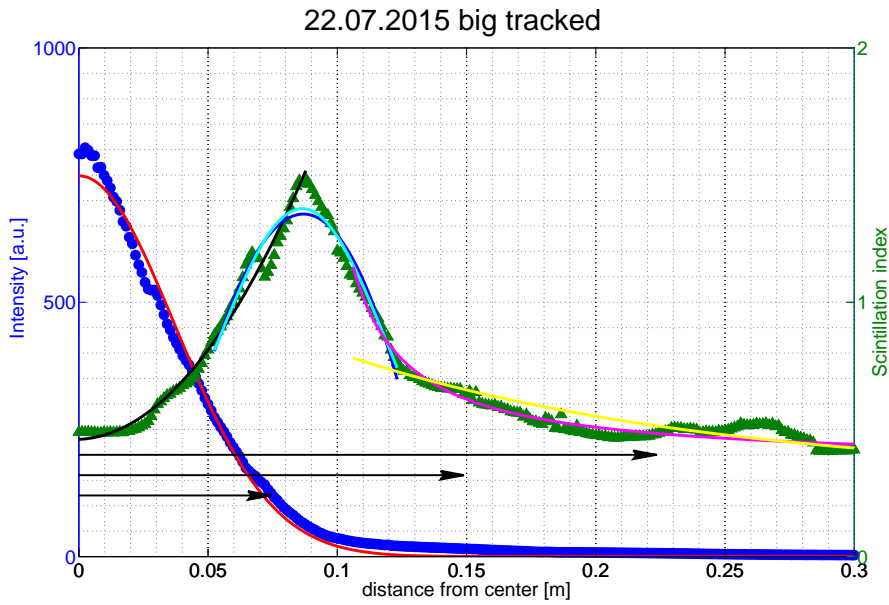


Figure 6.10: Measurement from 22.07.2015 with the small divergence collimator. In the post processing the beam was tracked. The arrows point to the single, double and triple beam radius. The mean field can be seen in blue and the Scintillationindex in green.

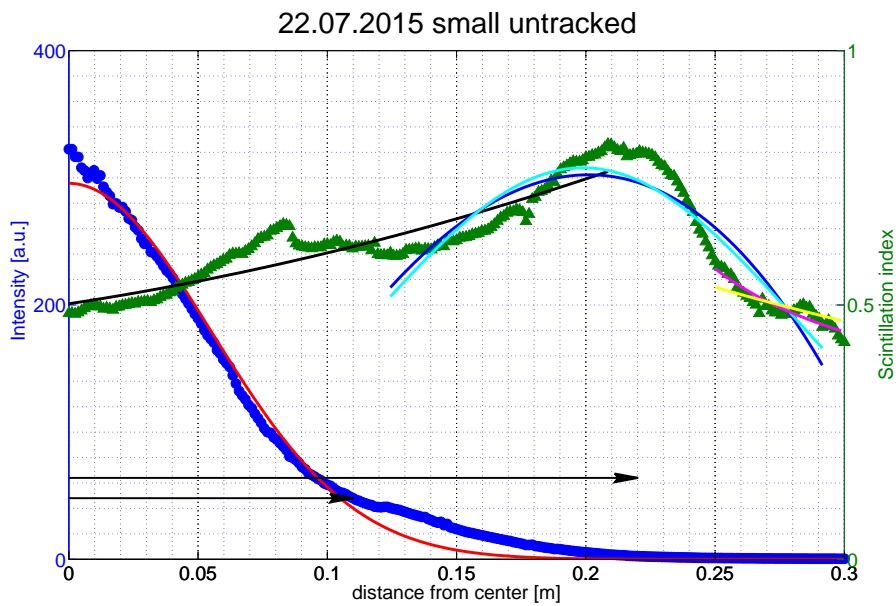


Figure 6.11: Measurement from 22.07.2015 with the big divergence collimator. The arrows point to the single and double beam radius. The mean field can be seen in blue and the Scintillationindex in green.

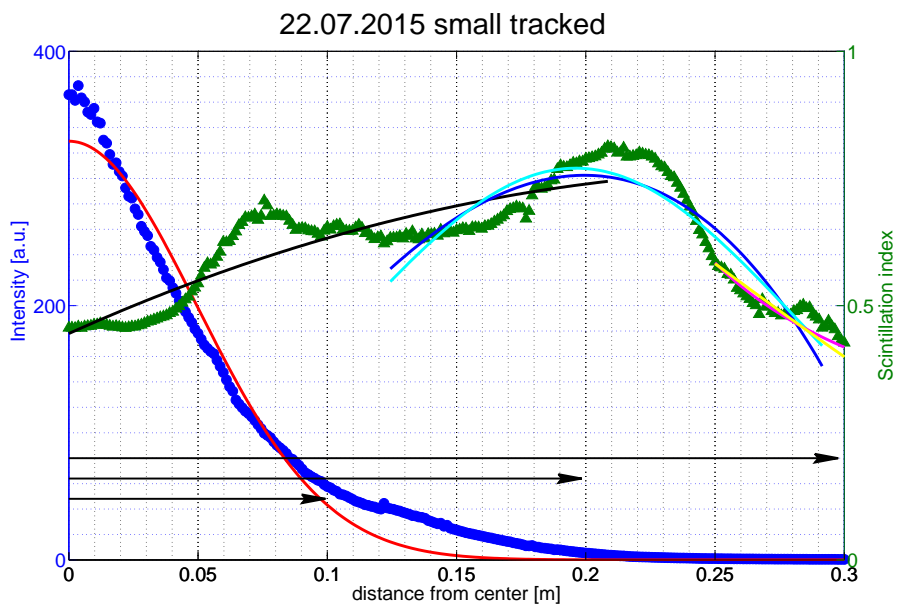


Figure 6.12: Measurement from 22.07.2015 with the big divergence collimator. In the post processing the beam was tracked. The arrows point to the single and double beam radius. The mean field can be seen in blue and the Scintillationindex in green.

6.4 Conclusion and Outlook

Even though the small collimator measurements do not show as significant characteristics as those done with the big collimator, they can be used to verify some theories. A surprising effect that can be shown in all the measurements is that the radial distance of the maximum scintillation index does not depend on tracking. Even more surprisingly, it does not seem to depend on the turbulence index either. Apparently, the distance is directly proportional to the divergence, but can not be connected to the beam size by a universal factor. The maximum scintillation index decreases slightly when tracking is activated. For a given divergence, it appears as though the maximum scintillation index and the on-axis scintillation index are connected by a factor which depends on the beam divergence. This factor increases with decreasing divergence and vice versa. Interestingly, it could be shown reproducibly that each measurement of the big collimator has a weak side peak close to the maximum. The cause for this effect has yet to be determined. Far enough off-axis, the scintillation index seems to reach a saturation value. The steepness of the decrease after the maximum depends on the turbulence index: the higher C_n^2 , the steeper the decrease. The saturation value of the scintillation index appears to be around the on-axis value.

To get a deeper understanding and to be able to quantify the observed effects, more measurements and more different collimators are required. The data clearly shows that the applied methods of measuring and post-processing are suitable for the purpose of getting the characteristics of off-axis scintillation and for finding basic correlations.

Chapter 7

Appendix

Bibliography

- [1] M. de los Reyes. <http://astro.physics.ncsu.edu/~madelosr/background.html>. [Online; accessed 3-January-2016].
- [2] L. C. Andrews and R. L. Phillips, *Laser beam propagation through random media*, vol. second edition. SPIE Press, 2005.
- [3] B. Mellish. <https://upload.wikimedia.org/wikipedia/commons/thumb/5/53/GaussianBeamWaist.svg/1280px-GaussianBeamWaist.svg.png>. [Online; accessed 11-August-2015].
- [4] L. C. Andrews and R. L. Phillips, “Recent results on optical scintillation in the presence of beam wander,” *SPIE*, vol. 6878, 2008.
- [5] S. T. Tamasflex. <https://upload.wikimedia.org/wikipedia/en/2/2c/Cassegrain.en.png>. [Online; accessed 11-August-2015].
- [6] Thorlabs. http://www.thorlabs.de/images/TabImages/LD_Collimation_dwg.gif. [Online; accessed 11-August-2015].
- [7] D. S. Mader. <https://upload.wikimedia.org/wikipedia/en/5/56/Shear-plate.png>. [Online; accessed 11-August-2015].
- [8] U. of Arizona. http://fp.optics.arizona.edu/opti471B/Reading/lab4/MG_ShearPlate_Theory_Application.pdf. [Online; accessed 11-August-2015].
- [9] Shigeru23. https://upload.wikimedia.org/wikipedia/commons/e/e2/LD_cut_model_2_E.PNG. [Online; accessed 11-August-2015].
- [10] Newport. <http://assets.newport.com/web900w-EN/images/8063.jpg>. [Online; accessed 03-August-2015].
- [11] Newport. <http://assets.newport.com/web600w-EN/images/1272175.gif>. [Online; accessed 06-August-2015].
- [12] A. Harris, J. J. Sluss Jr., and H. H. Refai, “Alignment and tracking of a free-space optical communicatios link to a uav,” *IEEE*, 2005.

-
- [13] J. D. Shelton, "Turbulence-induced scintillation on gaussian-beam waves: theoretical predictions and observations from a laser-illuminated satellite," *Optical Society of America*, 1995.
- [14] F. Dios, J. A. Rubio, A. Rodriguez, and A. Comerón, "Turbulence-induced scintillation on gaussian-beam waves: theoretical predictions and observations from a laser-illuminated satellite," *Optical Society of America*, 1995.
- [15] L. C. Andrews and R. L. Phillips, "Impact of scintillation on laser communication systems recent advances in modeling," *SPIE*, vol. 4489, 2002.
- [16] L. C. Andrews, R. L. Phillips, R. J. Sasiela, and R. Parenti, "Beam and effects on the scintillation index of a focused beam," *SPIE*, vol. 5793, 2005.
- [17] L. C. Andrews, R. L. Phillips, and P. Yu, "Optical scintillations and fade statistics for a satellite-communication system," *Applied optics*, vol. 34, 1995.
- [18] L. C. Andrews, R. L. Phillips, and P. Yu, "Optical scintillations and fade statistics for a satellite-communication system," *Applied optics*, vol. 34, 1995.
- [19] M. Charnotskii, "Weak and strong off-axis beam scintillations and beam wander for propagation in turbulence," *SPIE*, vol. 7685, 2010.
- [20] L. C. Andrews, W. B. Miller, and J. Ricklin, "Effects of the refractive index spectral model on the irradiance variance of a gaussian beam," *Optical Society of America*, vol. 11, 1994.
- [21] R. J. Kerr and J. R. Dunphy, "Experimental effects of finite transmitter apertures on scintillations," *Optical Society of America*, vol. 63, 1973.
- [22] J. C. Ricklin and F. M. Davidson, "Atmospheric optical communication with a gaussian schell beam," *Optical Society of America*, vol. 20, 2003.
- [23] 4th International Workshop on Optical Wireless Communications (IWOW), Istanbul, Sept. 2015, *Experimental characterization of intensity scintillation in the LEO downlink - Analysis of measurements during the KIDDO campaign*.
- [24] F. Moll, A. Shrestha, and C. Fuchs, "Ground stations for aeronautical and space laser communications at german aerospace center," *Proc. SPIE 9647*, 2015.

Acronyms

DLR German Aerospace Center.

FSO Free Space Optics.

IR infrared.

PDF joint probability density function.

PSD power spectral density function.

TOGS transportable optical ground station.

List of symbols

C_n^2 index of refraction structure constant.

L_0 outer scale of turbulence.

W beam radius.

W_0 minimal beam radius.

W_{LT} long term beam radius.

σ_R^2 Rytov variance.

l_0 inner scale of turbulence.

n Refractive index.

Re Renolds's number.

List of Figures

2.1	Three regions of turbulence. Source: [1].	5
2.2	Gaussian Beam principle. Source: [3].	9
2.3	Wandering of the instantaneous beam center. Source: [2].	12
2.4	Separation of the two beam wander effects. Source: [2]	13
2.5	Broadened beam after propagating through turbulent media. Source: [2]	13
2.6	Scintillation index off-axis (simulation). Source: [4]	16
3.1	Principle of a Cassegrain telescope. Source: [5].	17
3.2	Picture of the Cassegrain telescope at the measuring site.	18
3.3	Principle of a collimator. Source: [6].	19
3.4	Principle of a shearing interferometer. Source:[7].	20
3.5	Orientation of the fringes dependent on the beam characteristic Source: [8].	21
3.6	Principle of a laser diode. Source: [9].	21
3.7	Aerial view of the test link site.	22
3.8	Rough estimation of the Scintillation index for a collimator with large divergence. The short arrow marks $\pm W_{LT}$, whereas the long arrow marks $\pm 3 \cdot W_{LT}$	24
3.9	View of the telescope (black rings). The blue ring shows the beam at W_{LT} and the green ring shows $3W_{LT}$	24
3.10	Rough estimation of the Scintillation index for a collimator with small divergence. The short arrow marks $\pm W_{LT}$, whereas the long arrow marks $\pm 3 \cdot W_{LT}$	26
3.11	View of the telescope (black rings). The blue ring shows the beam at W_{LT} and the green ring shows $3W_{LT}$	26
4.1	Newport stage. Source: [10].	27
4.2	Collimator mounted on the stage in the rack.	29
4.3	1.concrete roof; 2.bitumen water sealing; 3.rubber plates layer; 4.alloy plate; 5.19- inch rack.	30
4.4	Rack standing on alloy plates laying on the rubber layer of the roof.	30
4.5	The whole picture represents the sensor area of the camera. The small magnifica- tion means bad usage of this area.	30
4.6	Interference pattern.	31
4.7	Pupil meanfield with the camera problem. In the middle of the beam the intensity is decreasing instead of increasing as would be expected for a Gaussian beam.	32
4.8	Blindspot in the middle of the beam. The small black spot in the middle of the beam shows no intensity at all.	32
4.9	Camera behavior. The graph shows the correlation between intensity on the chip of the camera and the converted ADC value, which causes the problem.	33

4.10	Radial meanfield when the camera problem shows up.	33
4.11	Histogram after 5000, 4000, 3000 and 2000 frames. It can clearly be seen that the shape of the distribution is not changing with the number of frames. This shows that 2000 frames are sufficient and additional images provide no additional information.	34
4.12	Meanfield of a preliminary measurement.	35
4.13	Scintillation index of a preliminary measurement.	35
5.1	Final setup.	36
5.2	Improved big magnification. The area of the camera is far better utilized than before.	37
5.3	Collimation of light from a point. Source: [11]	37
5.4	Aiming through the scope to place the beam on the primary telescope mirror. . .	40
5.5	Background radiation. This signal is a result of ambient light only.	41
5.6	Clipping frame. The dark red area shows the position of pixels repeatedly providing no valid data.	42
5.7	Meanfield of the new magnification. The Gaussian distribution of the beam can be seen very clearly.	42
5.8	Beamwander frame. The closer to yellow or even red a pixel is, the more often the beam center was located at that point in a single frame. Here the distribution of the beam wander can be seen.	43
5.9	Pattern which shows the area of valid data.	43
5.10	Scintillation index. It can be seen that the scintillation index rises away from the center.	44
5.11	Radial dependence of the mean field and the scintillation index for one single integration time of the camera.	44
5.12	Outcome of all radial dependencies of the mean field and Scintillation index plotted at once before they were sticking together. The mean field appears in red and the scintillation index in blue.	45
5.13	Here the radial dependencies of the mean field and the scintillation index after matching of the graphs can be seen. The scintillation index is depicted in green an the mean field in blue.	45
6.1	Measurement from 20.07.2015 with the small divergence collimator. The arrows point to the single, double and triple beam radius. The mean field can be seen in blue and the Scintillationindex in green.	47
6.2	Measurement from 20.07.2015 with the small divergence collimator. In the post processing the beam was tracked. The arrows point to the single, double and triple beam radius. The mean field can be seen in blue and the Scintillationindex in green.	47
6.3	Measurement from 20.07.2015 with the big divergence collimator. The arrows point to the single, double and triple beam radius. The mean field can be seen in blue and the Scintillationindex in green.	48
6.4	Measurement from 20.07.2015 with the big divergence collimator. In the post processing the beam was tracked. The arrows point to the single, double and triple beam radius. The mean field can be seen in blue and the Scintillationindex in green.	48

6.5	Measurement from 21.07.2015 with the small divergence collimator. The arrows point to the single, double and triple beam radius. The mean field can be seen in blue and the Scintillationindex in green.	50
6.6	Measurement from 21.07.2015 with the small divergence collimator. In the post processing the beam was tracked. The arrows point to the single, double and triple beam radius. The mean field can be seen in blue and the Scintillationindex in green.	50
6.7	Measurement from 21.07.2015 with the big divergence collimator. The arrows point to the single, and double beam radius. The mean field can be seen in blue and the Scintillationindex in green.	51
6.8	Measurement from 21.07.2015 with the big divergence collimator. In the post processing the beam was tracked. The arrows point to the single and double beam radius. The mean field can be seen in blue and the Scintillationindex in green.	51
6.9	Measurement from 20.07.2015 with the small divergence collimator. The arrows point to the single, double and triple beam radius. The mean field can be seen in blue and the Scintillationindex in green.	52
6.10	Measurement from 22.07.2015 with the small divergence collimator. In the post processing the beam was tracked. The arrows point to the single, double and triple beam radius. The mean field can be seen in blue and the Scintillationindex in green.	53
6.11	Measurement from 22.07.2015 with the big divergence collimator. The arrows point to the single and double beam radius. The mean field can be seen in blue and the Scintillationindex in green.	53
6.12	Measurement from 22.07.2015 with the big divergence collimator. In the post processing the beam was tracked. The arrows point to the single and double beam radius. The mean field can be seen in blue and the Scintillationindex in green.	54

List of Tables

5.1	Camera settings for the low divergence collimator.	39
5.2	Camera settings for the high divergence collimator.	39
6.1	Results for the measurements on 20.07.2015	46
6.2	Results for the measurements on 21.07.2015	49
6.3	Results for the measurements on 22.07.2015	52
7.1	Results for the measurements on 20.07.2015	63
7.2	Results for the measurements on 21.07.2015	64
7.3	Results for the measurements on 22.07.2015	65

Fitting Values

	small untracked			small tracked			big untracked			big tracked		
	A	B	C	A	B	C	A	B	C	A	B	C
Meanfield												
$A \cdot e^{x^2/2B^2}$	7177	0.041		7678	0.038		10262	0.037		11571	0.035	
Scintillationindex												
1 st part $A \cdot x^2 + B \cdot x + C$	63.8	-1.99	0.31	49.42	0.31	0.26	128.24	2.06	0.32	104.82	4.24	0.19
2 nd part: $A \cdot x^4 + B \cdot x^2 + C \cdot x$	469	-194.19		1417	-295.2		5066	-1039.18		7914	-1046	
2 nd part: $A \cdot e^{(x-B)^2/2C^2}$	1.11	1.11	0.146	0.05	1.1	0.145	0.06	1.41	0.087	0.03	1.28	0.087
3 rd part $A + B^{C \cdot x}$	0.18	1.13	-34.98	0.17	1.13	-34.98	0.44	1.43	-34.98	0.46	1.45	-34.98

Table 7.1: Results for the measurements on 20.07.2015

	small untracked			small tracked			big untracked			big tracked		
	A	B	C	A	B	C	A	B	C	A	B	C
Meanfield												
$A \cdot e^{x^2/2B^2}$	360	0.061		367	0.059		802	0.039		836	0.038	
Scintillationindex												
1 st part $A \cdot x^2 + B \cdot x + C$	-1.54	0.68	0.12	8.64	0.05	0.12	57.52	-1.67	0.16	50.31	-1.1	0.15
2 nd part: $A \cdot x^4 + B \cdot x^2 + C \cdot x$	109	-32.29		-529	4.35		-1841	-89.46		4769	-415.9	
2 nd part: $A \cdot e^{(x-B)^2/2C^2}$	0.19	0.163	0.09	0.2	0.1	0.06	0.43	0.088	0.03	0.42	0.089	0.03
3 rd part $A + B^{C \cdot x}$	0.11	1.67	-34.98	0.13	1.84	-34.99	0.1	1.62	-34.98	0.10	1.65	-34.98

Table 7.2: Results for the measurements on 21.07.2015

	small untracked			small tracked			big untracked			big tracked		
	A	B	C	A	B	C	A	B	C	A	B	C
Meanfield												
$A \cdot e^{x^2/2B^2}$	296	0.055		329	0.049		625	0.043		748	0.037	
Scintillationindex												
1 st part $A \cdot x^2 + B \cdot x + C$	2.27	0.77	0.5	-4.07	2.28	0.45	112	0.92	0.57	132	0.44	0.46
2 nd part: $A \cdot x^4 + B \cdot x^2 + C \cdot x$	-60.5	-26.3		-86	-16.7		-11404	-16.5		-1599	-399.2	
2 nd part: $A \cdot e^{(x-B)^2/2C^2}$	0.77	0.2	0.08	0.77	0.2	0.09	1.42	0.086	0.03	1.37	0.086	0.03
3 rd part $A + B^{C \cdot x}$	0.14	1.11	-34.98	0.31	0.42	4.94	0.3	1.21	-34.98	0.30	1.22	-34.98

Table 7.3: Results for the measurements on 22.07.2015